



Lawrence Berkeley Laboratory

UNIVERSITY OF CALIFORNIA

RECEIVED

LAWRENCE
BERKELEY LABORATORY

OCT 22 1984

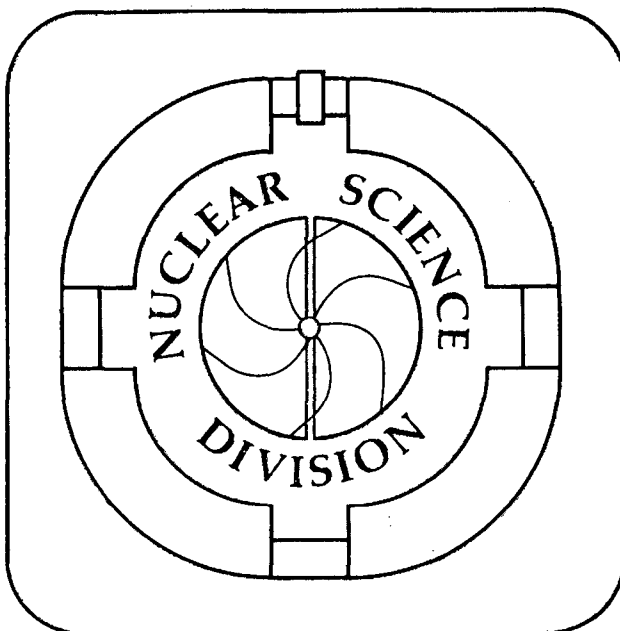
LIBRARY AND
DOCUMENTS SECTION

Submitted to Physical Review C

PRODUCTION MECHANISM OF BACKWARD ENERGETIC
PROTONS STUDIED FROM TWO-PARTICLE CORRELATIONS
IN 800 MeV PROTON-NUCLEUS COLLISIONS

Y. Miake, H. Hamagaki, S. Kadota, S. Nagamiya,
S. Schnetzer, Y. Shida, H. Steiner and I. Tanihata

September 1984



For Reference

Not to be taken from this room

LBL-18346
c.1

DISCLAIMER

This document was prepared as an account of work sponsored by the United States Government. While this document is believed to contain correct information, neither the United States Government nor any agency thereof, nor the Regents of the University of California, nor any of their employees, makes any warranty, express or implied, or assumes any legal responsibility for the accuracy, completeness, or usefulness of any information, apparatus, product, or process disclosed, or represents that its use would not infringe privately owned rights. Reference herein to any specific commercial product, process, or service by its trade name, trademark, manufacturer, or otherwise, does not necessarily constitute or imply its endorsement, recommendation, or favoring by the United States Government or any agency thereof, or the Regents of the University of California. The views and opinions of authors expressed herein do not necessarily state or reflect those of the United States Government or any agency thereof or the Regents of the University of California.

**PRODUCTION MECHANISM OF BACKWARD ENERGETIC PROTONS
STUDIED FROM TWO-PARTICLE CORRELATIONS
IN 800 MeV PROTON-NUCLEUS COLLISIONS**

Y. Miake^{a)}, H. Hamagaki, S. Kadota, S. Nagamiya^{a)}, S. Schnetzer^{b)},
Y. Shida, H. Steiner^{c)}, and I. Tanihata

Institute for Nuclear Study, University of Tokyo,
Midori-cho, Tanashi-shi, Tokyo 188, Japan

and

Nuclear Science Division, Lawrence Berkeley Laboratory,
University of California, Berkeley, California 94720, USA

ABSTRACT

The production mechanism of backward energetic protons has been studied in 800 MeV proton-nucleus collisions from measurements of two-particle coincidences over a wide kinematical region. Backward energetic protons ($P \geq 350$ MeV/c) at $\theta = 118^\circ$ were measured in coincidence with particles emitted in the angular range from 15° to 100° . Both in-plane ($\Delta\phi = 180^\circ$) and out-of-plane ($\Delta\phi = 90^\circ$) coincidences were measured.

The production of backward protons has been decomposed into several components depending on the excitation energy of the residual nucleus. Momentum spectra, angular distributions, and target mass dependences of these components as well as the associated particle multiplicity with the backward protons are studied. An importance of the scattering of the incident proton by the correlated nucleon clusters is suggested.

From the proton spectrum associated with the p-d quasi-elastic scatterings (QES), the momentum spread of the pn system ("d") inside the nucleus has been determined. The momentum spread of the "d" obtained by the p-d QES is found to be smaller than the spread observed in heavy-ion projectile fragmentation into deuterons. From the mass dependence of the ratio of the p-d to p-p QES cross sections, the mean free path of deuterons inside the nucleus has been determined.

NUCLEAR REACTIONS: p+C, p+NaF, p+KCl, p+Ag, and p+Pb, $E_p = 800$ MeV; measured $\sigma_1(P, \theta)$ and $\sigma_2(P_1, \theta_1, P_2, \theta_2)$; p-p QES and p-d QES.

PACS numbers : 25.40 -h

1. INTRODUCTION

The study of energetic proton-nucleus interactions may reveal effects of correlated nucleons in nuclear matter. Frankel et al. measured the inclusive spectra of backward protons and other light particles from 600-800 MeV proton-nucleus collisions.¹ Energetic protons far beyond the Fermi energy were observed. Many models were soon proposed to explain the backward emission mechanism of these energetic protons.

Amado and Woloshyn analyzed backward energetic protons(BEP) in terms of single nucleon-nucleon scattering.² They assumed that the backward emission of nucleons, which is forbidden in free nucleon-nucleon scattering, is due to the Fermi motion of a nucleon. They, however, showed that the single nucleon-nucleon scattering model with a conventional Fermi momentum distribution (Gaussian type) gives a cross section which is a few orders of magnitude smaller than the observed one. In other words, the observed spectrum requires a high-momentum tail of the Fermi momentum distribution in addition to the Gaussian type.

In the frame work of the single-scattering model, Frankel et al. introduced the concept of Quasi-Two-Body Scaling.³⁻⁹ Using this scaling they claimed that the BEP spectrum is reproduced with an exponential type Fermi momentum distribution, $\exp(-k/k_0)$ with $k_0 \approx 90$ MeV/c. An interpretation of the scaling are discussed based on an optical approximation by other authors.¹⁰

A correlated-cluster model proposed by Fujita et al.¹¹⁻¹⁴ and a fluctuon model proposed by Baldin et al.¹⁵ are also successful in explaining the inclusive spectra of BEP. These models are based on the idea that a large momentum can be transferred to the proton by a scattering of the incident proton off a heavier object such as a two- or three-nucleon cluster inside the target nucleus.

Another extreme idea is the statistical model.¹⁶ Knoll showed that the main features of BEP were reproduced by the statistical model, in which BEP are emitted from a statistically equilibrated nucleon system. He concluded that four target nucleons contribute to BEP production on average.

The models proposed so far, namely the single-scattering model, the correlated-cluster model, and the statistical model, mutually conflict in their basic assumptions, although all of them have explained the observed inclusive spectra.

Two types of measurements are expected to clarify this situation: a polarization measurement and a two-particle correlation measurement. Frankel and Woloshyn¹⁷ argued that an experiment with polarized protons is useful to distinguish the different models. Only the single-scattering model gives a large polarization of BEP, while the correlated-cluster model and the statistical model give small or no polarizations. The measurement was done by Frankel et al.¹⁸ using polarized 800 MeV protons. The analyzing power of protons emitted at around 100° was generally small, although it depends slightly on the target mass and on the momentum of the BEP. However, since the analyzing power is very sensitive to the final state interactions as well as to the details of the initial and the final state wave functions, no definitive statements on the production mechanism of BEP could be made.

Komarov et al. measured two-proton correlations at a beam energy of 640 MeV.¹⁹⁻²¹ They used a ΔE -E counter telescope to detect BEP in the momentum range from 310 to 530 MeV/c. A range counter telescope was used for the detection of forward particles in the momentum range from 730 to 850 MeV/c. When BEP is emitted through the scattering of an incident proton on a deuteron inside the nucleus, the scattered deuteron comes out either in the form of a deuteron or two nucleons (p and n). The energy window of forward protons in Komarov's experiment was very limited and covered only the energy region of protons which are emitted through the deuteron breakup with only a small relative momentum between proton and neutron. Two-nucleon clusters other than a deuteron may exist inside the nucleus such as p-p, n-n, or p-n singlet. Thus, the idea was expanded to the p-(2N) scatterings, where (2N) symbolically indicates two-nucleon clusters. They concluded that the cluster scattering of the incident proton is the main mechanism of the BEP production.

Frankel et al.²² also measured two proton correlations in $p+{}^6\text{Li}$ reactions at proton energies of 600 and 800 MeV. They observed quasi-elastic scatterings of protons from

${}^6\text{Li}$ as well as coincidence events between forward and backward protons at the p-(2N) scattering kinematics. However, their energy and angular range was very restricted.

As described above, three mechanism have been proposed so far for production of BEP. Also, experimental attempts have been undertaken to separate one mechanism from the others. Currently, however, it is not yet clear whether these mechanism conflict mutually or whether they can coexist. Also there is little experimental indication if one of these mechanism is more important than the others.

To make our question clearer, let us write down the mechanism of BEP production as follows:

$$p + nN \rightarrow p(\text{backward}) + m + \dots \quad (1.1)$$

Here, the incident proton is scattered by a n-nucleon cluster inside the target nucleus, and after the collision a backward proton and m-particles, usually at forward angles, are emitted. The three mechanisms described above correspond to $n=1$ for the single scattering model, $n \geq 2$ for the correlated cluster model, and $n=\text{large}$ for the statistical model.

We now show that from two particle coincidences between p(backward) and m(forward) the above three mechanism are kinematically separable from each other. In p-p coincidences, if two protons satisfy the condition of $E_B + E_F \approx E_{\text{beam}}$, then these two protons are mainly from a p-p quasi-elastic scattering between the projectile proton and a proton inside the target nucleus, and thereby, from the $n=m=1$ process. (Subscripts, B and F refer to backward and forward, respectively and E refers to kinetic energy.) Similarly, the p-d coincidence under the condition of $E_B + E_F \approx E_{\text{beam}}$ selects p-d quasi-elastic scatterings, and thus, the $n=2, m=1$ process.

In-plane and out-of-plane indicate that the azimuthal separation, $\Delta\phi$, between the two detected particles is 180° and 90° respectively. Since the statistical model implicitly assumes that each particle experiences incoherent multiple nucleon-nucleon collisions, the azimuthal asymmetry tends to be wiped out.

Obviously, in the proton-cluster collision, clusters may break up into nucleons. These reactions are marked by the fact that $E_B + E_F \neq E_{\text{beam}}$ and therefore, again

separable. The kinematical separation of these processes is illustrated in Fig. 1 together with the kinematical region covered by the present experiment:

The previous trials of measuring two-particle coincidences by Komarov et al. and by Frankel et al. did not cover a kinematic domain wide enough to allow us to study the question raised above. Recently a coincidence experiment which covers a wider kinematical range was reported for 300 MeV incident protons.²³ They observed contributions from quasi elastic scatterings as well as multiple scatterings. However the relative importance of those components is not clear yet.

In the present experiment, we have measured two-particle coincidence spectra under both in-plane and out-of-plane coincidence conditions. Coincidence events between p(backward) and p(forward) as well as p(backward) and d(forward) have been measured over a wider kinematic domain shown by a hatched rectangle in Fig. 1. From the detection of these particles, our intention is to kinematically select each process and then to quantitatively evaluate its contribution to BEP.

In the present experiment the p-d quasi-elastic scatterings at large momentum transfer have been measured as well. These data are related to the short range behavior of two-nucleon clusters.¹¹⁻¹⁵ We will discuss the width of the momentum distribution of the pn system inside the nucleus.

2. EXPERIMENTAL ARRANGEMENTS AND PROCEDURES

2.1 General

In the present experiment, the spectra of backward protons in coincidence with forward going particles were measured in 800 MeV proton nucleus collisions. Backscattered protons in the momentum range 330-700 MeV/c were detected at scattering angles from 103° to 153° , and forward protons and deuterons of a momentum range 480-2000 MeV/c were detected at scattering angles 15, 20, 30, 40, 55, 70, 90, and 100 degrees. Although we have measured coincidence spectra at various angles, we put our

emphasis on the coincidence data between 118° and 15° , because this angular combination includes both p-p and p-(2N) scattering kinematics as shown in Fig. 1.

A magnetic spectrometer was used to detect forward particles. The spectrometer, which has an angular acceptance of $\Delta\theta = 8^\circ$, was rotated from 15° to 100° at $\phi=0^\circ$ (definition of ϕ). Two sets of $\Delta E-E$ telescopes were used to detect backward protons. One telescope was set at $\phi=180^\circ$, in the same reaction plane with the spectrometer, and the other was set at $\phi=90^\circ$. The counter setup as well as the coordinate definition is illustrated in Fig. 2. Performance of the detectors are summarized in Table 1.

2.2 Beam and Targets

We used an 800 MeV proton beam accelerated by the Bevatron at Lawrence Berkeley Laboratory. Typically the beam intensity was 10^7 to 10^8 particles per pulse and the beam repetition period was 6 seconds. The duration of each beam pulse was about 600 ms.

Discs of C, NaF, KCl, Ag, and Pb with 5 cm in diameters were used as targets. A typical thickness was about 0.5 g/cm^2 . The energy loss of protons in these targets was much smaller than the energy resolutions of the detectors.

The beam intensity was monitored by an ionization chamber (IC) inserted in the beam line at 1.5 m upstream of the target. The IC was filled with a mixed gas of 80% Ar and 20% CO_2 at 1.05 atm. The total charge collected in the IC was measured for every beam pulse. The background charge of IC was measured during the beam-off period. For the calibration of the IC, we placed two thin plastic scintillation counters in the beam, and measured the charge collected in the IC against the coincidence counts between these two counters at low beam intensity ($10^3 - 10^6$ particles). At high beam intensity we used a monitor counter telescope (MC) which counted scattered particles from a target. The counting rate of the MC was compared with the charge of the IC. The linearity between the collected charge in the IC and the count of the MC was good within a few percent in the whole intensity range used in the experiment.

2.3 The $\Delta E-E$ counters

Backward-emitted particles were detected by plastic scintillation $\Delta E-E$ counter telescopes. Two sets of telescopes covered an angular range of $\theta = 105^\circ - 155^\circ$, one at $\phi = 180^\circ$ (RB) and the other at $\phi = 90^\circ$ (UB). Figure 3 shows a plan view of the telescope RB. The first counter (RB1) and the second counter (RB2) measured the energy loss (dE/dX) of a particle. Since RB2 had phototubes on both ends of the plastic scintillator, the hit position was also determined. The third counter (RB3) consisted of five energy(E) counters RB3a, RB3b, RB3c, RB3d, and RB3e and a veto counter RB3f. Each of these E counters covered $\Delta\theta = \pm 5^\circ$. The veto counter RB3f was used to reduce the background from stray beam particles.

A typical scatter plot of the pulse heights between ΔE and E counters is shown in Fig. 4. A clear separation of protons, deuterons, and pions is seen in the figure. The maximum proton momentum measured by the telescope was 700 MeV/c which was determined by the total thickness of the telescopes. The minimum proton momentum was 330 MeV/c. The probability of secondary reactions in the E counter was about 32% for a 700 MeV/c proton. The detection efficiency was not affected by the secondary reaction, whereas the pulse height was reduced and thus affected the energy resolution.

For energy calibration, we set the telescope behind a time of flight (TOF) counter with a flight length of 2 m. The velocity of a particle was measured by the TOF counter, and the dE/dX and the E were measured by the $\Delta E-E$ counter at the same time. Particle identification was done by the $\Delta E-E$ counter and the energy was determined from the proton velocity measured by the TOF counter. Figure 5 shows a result of the calibration. The E_{\min} and the E_{\max} written in Fig. 5 indicate the minimum and the maximum energies of the $\Delta E-E$ counter calculated by the range-energy relation. The momentum resolution was 9% at a proton momentum of 480 MeV/c and 8.5% at 700 MeV/c.

The effective solid angle of the telescope was estimated by a Monte Carlo calculation of multiple Coulomb scatterings. Because the first and the second counters (RB1 and RB2) had wider solid angles than the E counter, low energy protons could be kicked into the E counter by multiple scattering. Therefore the effective size of the E counter

is larger than the geometrical one. On the other hand, high energy protons escape from the side of the E counter, and the effective size become smaller. The effective solid angle as a function of proton energy is shown in Fig. 6.

2.4 The Magnetic Spectrometer

Forward emitted particles were detected by a magnetic spectrometer. The spectrometer was set at $\phi = 0^\circ$ and rotated from $\theta = 15^\circ$ to 100° . The magnetic spectrometer consisted of a C-magnet, a scintillation counter telescope, and multi-wire proportional chambers (MWPC). The bending angle in the magnetic field, the time of flight, and the pulse height of the plastic scintillation counters were measured in order to identify the particle and to determine its momentum. The momentum resolution of the spectrometer was governed by the wire spacing of the MWPC's for high energy particles and by multiple Coulomb scatterings in the plastic scintillation counters for low energy particles. The momentum resolution is listed in Table 2.

The magnetic spectrometer used in the present experiment is the same one as described in Ref. 24. A more detailed description of the spectrometer is given there.

2.5 Electronics and Data Acquisition System

We used two types of event triggers,

$$INCL = SPE + RB + UB \quad (2.1)$$

$$COIN = SPE * (RB + UB) \quad (2.2)$$

where "*" means logical AND and "+" means logical OR. Symbols SPE, RB, and UB indicate the signals of the magnetic spectrometer, the $\Delta E-E$ telescope RB, and UB, respectively. The trigger INCL refers to the single-particle inclusive measurement and COIN to the two-particle coincidence measurement. The coincidence $SPE * RB$ detect the in-plane emission ($\Delta\phi = 180^\circ$) of two particles and the $SPE * UB$ for the out-of-plane emission ($\Delta\phi = 90^\circ$).

We monitored the accidental coincidence rate of each telescope by counting the coincidence in which timing was shifted by about 200 ns. The accidental coincidence was typically 2% of the real coincidence. Even though these accidental coincidences

were accepted as trigger events, most of these events were rejected at the stage of consistency checks in the off-line analysis. The fraction of accidental coincidence between two different detectors (SPE*RB and SPE*UB) were estimated from the coincidence resolving time (30 ns) and the microscopic duty factor of the beam. The mixture of the accidental two-particle coincidence was found to be less than 5 %.

For on-line data taking, we used an MBD-11 (micro-programmable branch driver) which was connected to a PDP-11/20 computer. All the information of the pulse height(ADC), the timing (TDC), the multi-wire proportional chamber reading, and the scalers was recorded onto magnetic tapes through three CAMAC crates connected to the MBD-11. In order to monitor each counter, on-line data analysis was performed during the beam off period. Histograms and scatter plots of any desired combinations of the ADC, TDC, wire-chamber's hit pattern, and bending angle distribution were displayed during the run in order to check if the system was working properly. The contents of scalers were also monitored. Off-line data analysis was done by a VAX-11/780 at the Bevalac and by a FACOM M180-II-AD at the Institute for Nuclear Study of University of Tokyo.

3. EXPERIMENTAL RESULTS

We have measured in-plane and out-of-plane coincidence cross sections associated with backward protons. Protons and deuterons from 15° to 100° were detected in coincidence with the backward protons. For comparison the inclusive cross sections of backward protons were also measured. Conditions of these measurements are tabulated in Table 3. In this paper we present the data which essentially provide most of the physics information. The cross sections for the other cases that are not shown in this report may be obtained directly from the authors.

3.1 Inclusive Spectra of Backward Protons

Figure 7 shows examples of proton inclusive momentum spectra at $\theta = 118^\circ$ with C, KCl and Pb targets at an incident proton energy of 800 MeV. Protons from C, KCl, and Pb

show similar exponential type spectra. Error bars in the figure show only statistical errors. The systematic error of the absolute cross section was estimated to be less than 20%. The spectra can be parametrized by,

$$\frac{d^2\sigma}{dP d\Omega} = C_0 e^{(-P/P_0)}, \quad (3.1)$$

with the slope parameters P_0 ,

$$P_0 = 94 \pm 6 \text{ MeV/c} \quad \text{for C,} \quad (3.2)$$

$$P_0 = 87 \pm 4 \text{ MeV/c} \quad \text{for KCl, and} \quad (3.3)$$

$$P_0 = 85 \pm 4 \text{ MeV/c} \quad \text{for Pb.} \quad (3.4)$$

The slope parameter is independent of the target mass within errors. These values of the slope parameter are consistent with the previous data shown in refs. 1-6.

In Fig. 8 the momentum integrated cross sections, $d\sigma(\theta)/d\Omega$, are plotted as a function of the emission angle. Integration was done over the momentum range from 350 MeV/c to 700 MeV/c. Each datum point covers $\pm 5^\circ$ in θ . Again, protons from C, KCl, and Pb show a similar behavior.

In Fig. 9 $d\sigma(\theta)/d\Omega$ at $\theta = 118^\circ$ is plotted as a function of the target mass number A . The $d\sigma(118^\circ)/d\Omega$ can be parameterized by,

$$d\sigma(118^\circ)/d\Omega = 0.19 A^{1.0} \text{ (mb/sr)}. \quad (3.5)$$

The power in A is found to be constant within present angular range ($108^\circ - 148^\circ$). This power in A is larger than that of the total reaction cross sections ($\sim A^{2/3}$) and are consistent with previous data.^{17,21}

3.2 Momentum-Momentum Correlations

Figure 10 shows momentum-momentum (P_1 vs. P_2) scatter plots for in-plane(a) and out-of-plane(b) two protons one detected at $\theta_1 = 15^\circ$ and the other at $\theta_2 = 118^\circ$, respectively, in p+KCl collisions. The size of the circle in the figure indicates the number of events accumulated for $\Delta P_1 \times \Delta P_2 = 60 \text{ MeV/c} \times 20 \text{ MeV/c}$ bin. The solid curve in Fig. 10 shows the kinematical locus of p-p quasi-elastic scatterings. For drawing the curve we assumed 30 MeV binding energy for a proton inside the target nucleus. Numbers along

the curve indicate the momentum of the proton (in MeV/c) in the target nucleus. We see a ridge of the events along the curve. As we see from these value of internal momenta, events here originate mainly from quasi-elastic scatterings of protons with large internal momenta ($P_F \geq 300$ MeV/c).

A dashed line in Fig. 10 shows the kinematical locus of p-d quasi-elastic scatterings followed by the deuteron breakup into a proton and a neutron with zero relative momentum. We assumed 60 MeV binding energy by which deuterons are bound to the nucleus. Numbers beside the line indicate the internal momenta of deuterons. A dotted curve in the figure shows the kinematical locus of breakup of deuterons with zero internal momentum, but with finite relative momentum between the resulting proton and neutron. The crossing point between the dashed and dotted lines indicates the kinematical point where the deuteron with zero internal momentum breaks up into a proton and a neutron at zero relative momentum. A smooth and wide distribution of events are seen in both in-plane and out-of-plane coincidence. The out-of-plane coincidence events are concentrated more in the low momentum region.

Figure 11 shows in-plane(a) and out-of-plane(b) momentum-momentum scatter plots, respectively, between forward deuterons ($\theta_d = 15^\circ$) and backward protons ($\theta_p = 118^\circ$) in collisions of p+KCl. A clear peak near the kinematics of the p-d elastic scattering, which is shown by "+" in the figure, indicates the existence of p-d quasi-elastic scatterings.

3.3 A Classification of the Events

In p-p coincidence events, we used the excitation energy (E_{ex}) of the residual nuclear system, which contains (A-1) nucleons and possibly pions, as a parameter to classify the reaction mechanism.

The reaction is described as

$$p_i + A \rightarrow p_1 + p_2 + (A-1) ; \quad (3.6)$$

where p_i is the incident proton, p_1 and p_2 are the detected protons, A is the target nucleus with target mass number A, and (A-1) is the residual nuclear system. Here

(A-1) is not necessarily the ground state of the nucleus. The excitation energy (E_{ex}) of the residual nuclear system is defined by,

$$E_{ex} = (E_{A-1}^2 - P_{A-1}^2)^{1/2} - E_{g.s. \text{ of } A-1} \quad (3.7)$$

where E_{A-1} and P_{A-1} are given by,

$$E_{A-1} = E_i + E_A - E_1 - E_2, \quad \text{and} \quad (3.8)$$

$$\vec{P}_{A-1} = \vec{P}_i - \vec{P}_1 - \vec{P}_2, \quad (3.9)$$

where E_j is the total energy and \vec{P}_j the three dimensional momentum of the particle $j=i, 1, 2, A-1$, or A.

Number of events as a function of E_{ex} are plotted in Fig. 12. Solid circles in this figure represent the in-plane coincidence events and open circles the out-of-plane coincidence events. A difference between the IPC (in-plane coincidence) and the OPC (out-of-plane coincidence) is clearly seen in Fig. 12. The OPC events increases monotonically with E_{ex} , but the IPC shows a peak near $E_{ex}=0$ which corresponds to the p-p QES events. Because p-p QES induce two-proton emission in the same reaction plane, it is reasonable that the yield at $E_{ex} \approx 0$ is much higher for IPC than for OPC.

The other important feature here is the fact that the IPC shows larger number of events than the OPC by a factor of two in the region of $E_{ex}=200-400$ MeV. If the excitation energy is shared by many nucleons, the asymmetry is expected to be small. Therefore the observed fact suggests that the remaining energy is most likely shared by a small number of nucleons.

We now classify the coincidence events into three categories by the E_{ex} :

- (1) "p-p QES" ... IPC events with E_{ex} less than 100 MeV,
- (2) "p-p non-QES" ... IPC events with E_{ex} more than 100 MeV,
- (3) "p-p OPC" ... out-of-plane coincidence events.

Excitation spectra of the residual (A-2) nucleon system for the p-d coincidence events are shown in Fig. 13. A clear peak corresponding to the p-d QES is seen in the in-plane coincidence events. A similar classification is made for p-d events according to the E_{ex} of the event.

- (1) "p-d QES" ... IPC events with E_{ex} less than 100 MeV,
- (2) "p-d non-QES" ... IPC events with E_{ex} more than 100 MeV,
- (3) "p-d OPC" ... out-of-plane coincidence events.

3.4 Slope Factors of the Backscattered Protons

Figure 14 shows the backward proton spectra for three components of p-p coincidence events. Solid squares show the cross sections for "p-p QES". A solid line drawn in the figure is the fit to the data by,

$$\frac{d^3\sigma}{d\Omega_1 d\Omega_2 dP_2} = C_0 e^{(-P_2/P_0)}, \quad (3.10)$$

with $P_0 = 55 \pm 5$ MeV/c. The solid circles in Fig. 14 show the cross sections of protons classified as "p-p non-QES". The slope of the spectrum is less steep than that of "p-p QES"; P_0 is 91 ± 5 MeV/c in this case. Triangles in the figure show the cross sections of "p-p OPC". The value of P_0 of "p-p OPC" is 68 ± 6 MeV/c.

Figure 15 shows the momentum spectra of the backward protons of the p-d coincidence. The cross sections of protons classified as "p-d QES" spectrum shows a peak structure. The "p-d non-QES" spectrum shows an exponential shape with a slope factor P_0 of 94 ± 8 MeV/c. The slope factor of "p-d OPC" is 73 ± 7 MeV/c.

The slope factor of each component in p+KCl collisions is summarized in Table 4, in which the data from other angular combinations are also included as well as the slope factor of the inclusive spectrum at 118° . The slope factors are almost independent of the coincidence angle θ_1 except "p-p non-QES", where the slope factor decreases at larger angles. The similar dependence of the slope factor on the coincidence particle angle is observed for other targets. The target dependence of the slope factors is shown in Table 5 for the data at $\theta_1 = 15^\circ$ and $\theta_2 = 118^\circ$. The slope factors show small dependence on the target.

The value of P_0 for "p-p non-QES" agrees with the ones observed in inclusive spectra. This fact suggests a close relationship between these two spectra. The P_0 of "p-p OPC" is slightly smaller than that of inclusive. The P_0 of "p-p QES" is considerably

smaller than that of inclusive. An obvious conclusion here is that the momentum spectrum of "p-p QES" falls off much faster than the inclusive spectrum, and therefore, at high momentum "p-p QES" does not contribute to the inclusive spectrum as a main component.

3.5 The Momentum Integrated Cross Sections

To study the relative importance of each component, the two-particle cross sections were integrated over the momenta. The integration was made over the momentum range covered by the present detector system, namely $480 \leq P_1 \leq 2000$ MeV/c and $330 \leq P_2 \leq 700$ MeV/c. The integrated cross sections ($d^2\sigma/d\Omega_1 d\Omega_2$) thus obtained are listed in Table 6.

The θ_1 dependences of ($d^2\sigma/d\Omega_1 d\Omega_2$) are plotted in Fig. 16 and Fig. 17 for the KCl target. While "p-p QES" falls off rapidly with the emission angle of the forward proton, "p-p non-QES" and "p-p OPC" falls off slowly. One interesting feature of the data is that ratios of "p-p non-QES" to "p-p OPC" are nearly constant over the wide angular range. A similar behavior is observed in p-d coincidence data (Fig. 17).

The cross sections at $\theta_1 = 15^\circ$ and $\theta_2 = 118^\circ$ are also plotted as a function of the target mass number (A) in Fig. 18 and Fig. 19. Different components show different A-dependences. A weak A-dependence ($A^{0.5}$) observed in "p-p QES" is consistent with the idea that the quasi-elastic scatterings occur at the surface of the nucleus. Slightly stronger mass dependences are observed in "p-p non-QES" ($A^{0.6}$) and in "p-p OPC" ($A^{0.76}$). The component of "p-p OPC" increases most rapidly with target mass. The strong mass dependences may indicate that these components involve multi particles in their production mechanism. This idea is also consistent with the fact that the ratio of IPC/OPC is smaller for heavier target because more nucleons are likely to be involved in the collisions off heavier nuclei. The A dependence of the "p-p non-QES" ($A^{0.6}$) is much stronger than the $A^{0.39}$ observed by Komarov et al.²¹. In their experiment, a range counter telescope was used to detect the forward proton. We think that the application of the range telescope for high energy protons ($E \geq 300$ MeV) is somewhat doubtful.

As in the case of p-p events, the components of "p-d OPC" and "p-d non-QES" increase rapidly with target mass and "p-d QES" shows a weaker dependence. A detailed comparison of the A-dependence between p-p and p-d events will be discussed later.

4. DISCUSSIONS

4.1 Relative Importance of Each Component in Inclusive Spectra

In this section, the reaction mechanism responsible for the production of backward energetic protons is discussed. As in the previous sections, we classify the coincidence events into several categories. In order to estimate the relative contribution of each type to the inclusive spectra, we integrate the two-particle coincidence cross section ($d^2\sigma/d\Omega_1 d\Omega_2$) over θ_1 in collisions of p+KCl. Here, the integration along ϕ is left over since we have no detailed information on the ϕ distribution of the two-particle coincidence cross sections. The emission angle of the backward proton is fixed at $\theta_2=118^\circ$. For the integration from $\theta_1=0^\circ$ to 180° , the cross sections were extrapolated to smaller angles (from 0° to 15°) and to larger angles (from 100° to 180°). The error due to the extrapolation is less than 20%. The integrated cross sections σ_I of each component for p+KCl collisions listed in Table 7 have systematic errors of about 30% in the absolute values. Relative errors are less than 20%. It is clear that contributions from "p-p non-QES" and "p-p OPC" are the largest.

The slope factors of the backward proton spectra for different components are compared in Table 5. The "p-p QES" shows a smaller P_0 value than that of the inclusive spectrum with very small value of the integrated cross section. Therefore, the "p-p QES" component does not contribute significantly to the production of backward energetic proton.

As seen in Fig. 15 the cross section of "p-d QES" is almost as large as "p-d non-QES" at angles $\theta_d=15^\circ$ and $\theta_p=118^\circ$ in p+KCl collisions. With regard to the momentum spectra, the high momentum part of the backward proton of "p-d QES" gives about the same slope as that of the inclusive spectrum. This fact is consistent with the idea of cluster

scatterings. Therefore, "p-d QES" may contribute significantly to BEP production from light target nuclei. On the other hand the integrated cross sections of "p-d QES" are relatively small compared to the other components especially for heavier nuclei. A weak target mass dependence of "p-d QES" may be due to the fact that a deuteron produced through p-d QES is rescattered and breaks up into a proton and a neutron in heavier mass targets. The rescattering probability or the mean free path of the deuteron will be discussed later in section 4.3.2..

The slope factor (P_0) of the "p-p non-QES" and "p-p OPC" spectra are larger than that of "p-p QES" and the value of P_0 of "p-p non QES" is close to that of the inclusive spectrum. This fact suggests that "p-p non QES" contributes significantly to the production of BEP. It is also supported by the large cross section of this component. The value P_0 of "p-p OPC" is slightly smaller than that of the inclusive spectrum thus showing that "p-p OPC" can not be the main component at the highest momentum. From the integrated cross section, however, a significant contribution from "p-p OPC" is indicated in the present momentum range.

The associated multiplicity $\langle m \rangle$ is the average number of the particles which are emitted along with the back scattered proton, and is written as

$$\int \frac{d^2\sigma}{d\Omega_1 d\Omega_2} d\Omega_1 = \langle m \rangle \frac{d\sigma(incl)}{d\Omega_2}, \quad (4.1)$$

where Ω_2 refers to backward protons and Ω_1 refers to associated particles. For integrating two-particle coincidence cross sections over Ω_1 , we need to assume a ϕ distribution of the cross section. We have only two data points on ϕ distribution, one at $\phi=90^\circ$ as OPC events and the other at $\phi=180^\circ$ as IPC events. We assume that the ϕ distribution is linear in $\cos\phi$ to first order. The integrated cross sections σ_I are then,

$$\sigma_I \text{ of p-p coincidence} = 2.95 \text{ mb/sr},$$

$$\sigma_I \text{ of p-d coincidence} = 0.69 \text{ mb/sr}.$$

The $\langle m \rangle$ is calculated as

$$\langle m \rangle = (2\sigma_I(pp) + 2\sigma_I(pd)) / \sigma_{incl}. \quad (4.2)$$

The factor of 2 in front of $\sigma_I(pp)$ comes from the assumption that the number of

associated neutrons is the same as the number of associated protons. Using the inclusive cross section at $\theta=118^\circ$, $\sigma_{incl}=6.2$ mb/sr, we get $\langle m \rangle = 1.2$. The BEP are accompanied (on average) by 1.2 nucleons with momenta larger than 480 MeV/c. (The momentum 480 MeV/c is the lower momentum limit of the spectrometer in the present experiment.) This fact suggests that BEP are produced in reactions with a relatively small number of nucleons. If BEP are produced through multiple scattering with many nucleons, many low energy particles would be emitted. Although we have not observed particles with momentum less than 480 MeV/c, the extrapolation of the momentum spectra to zero momentum can be made by the fact that $d\sigma/dPd\Omega=0$ at $P=0$. A rough estimation based on this extrapolation (the extrapolation is made only for the associated particles) gives an integrated cross section about twice as large as the one obtained in our measured momentum range. The error due to the extrapolation is less than 30% for various methods of the extrapolation. As a result, the backward energetic proton is found to be associated with about 2.4 nucleons on average.

Figure 20 shows the backward proton spectra for "p-p non-QES" minus "p-p OPC" in collisions of p+KCl as compared with the spectrum of "p-d QES". Both spectra show peaks at around 430 MeV/c. The similarity of two distributions suggests that the basic reaction mechanism of "p-d QES" and the excess part of "p-p non-QES" are related each other. In Fig. 21 we also show contour lines of the cross section ($d^4\sigma/dP_1dP_2d\Omega_1d\Omega_2$) for p-p IPC events minus OPC events. Kinematical loci for p-p quasi-elastic scattering and for p-d quasi-elastic scattering are shown in the figure as well. A considerable number of events are distributed along the kinematical locus of p-d which presumably correspond to p-(2N) reactions followed by the breakup into nucleons.

Now we summarize the present study for the backward mechanism. In Table 8 we summarize the various observed values, namely the slope factors (P_0) of the backward proton spectra ($\theta=118^\circ$), the power in A of the cross sections, and the average multiplicities of the coincidence and the inclusive events. The following information is drawn from the data.

- (1) The emission of backward protons ($350 \leq P \leq 700$ MeV/c at 118°) is predominantly associated with nucleons. The contribution from the deuteron coincidence is about 10-20%. The contribution from associated particles with mass number greater than two is very small.
- (2) Among the proton associated events, the nucleon-nucleon quasi-free scattering gives only a small contribution.
- (3) The large in-plane to out-of-plane asymmetry and the small associated multiplicities indicate that backward protons are emitted mainly through the reaction in which only a few, most likely two or three, target nucleons are involved.
- (4) The excess part of the in-plane p-p coincidence to the out-of-plane p-p coincidence shows the same behavior as p-d QES. Therefore this part of the cross section is considered to be from the reaction in which the incident proton scattered off a (2N) system inside the target nucleus.

Summarizing the above information, it is considered that the main part of the backward protons is emitted by p-(2N) cluster scatterings. Namely, an incident proton collides with a two-nucleon cluster inside the target nucleus in the first stage. Then, one of the scattered protons, most likely a proton that originally belonged to the cluster, is emitted at a large angle leaving two other nucleons moving forward at high energies. Although these two nucleons occasionally emerge as a deuteron, they are mostly emitted as two separated nucleons. Occasionally one or two of these nucleons might be rescattered by other nucleons to produce low energy nucleons. These nucleons, however, cannot be observed by the present experimental device. It is worth mentioning that a possibility of incoherent multiple scattering with a few nucleons is, in principle, not rejected within the framework of the present data. However the number of target nucleons involved in the cascading process which produces energetic backward protons, was estimated by a phase space model ¹⁶ to be about four. The measured associated multiplicity of 2.4 is somewhat smaller than this value. This may imply that cluster scattering is more favored than the random cascade process.

Finally, if there are short range correlated clusters of three nucleons, these effects would show up at angles larger than 15° . Multi-nucleon clusters would, however, breakup more easily in a heavier target. In the present experiment, we also collected p-t events, but, statistics are too poor to discuss their contribution.

4.2 p-p Quasi-Elastic Scatterings

We make a simple comparison of the "p-p QES" data to plane-wave impulse approximation(PWIA) calculations. Because the counter system did not have enough momentum resolution to separate the individual states of the residual nuclei, the component of "p-p QES" includes contributions from various final states. Therefore an effective Fermi momentum distribution was used instead of the momentum distribution obtained by the shell model wave functions. We assumed the Fermi momentum distribution to be a Gaussian,

$$F(P)dP^3 = \text{const.} \times \exp(-P^2/2\sigma_p^2)dP^3, \quad (4.3)$$

where σ_p is 108.2 MeV/c, which corresponds to a Fermi momentum of 240 MeV/c. The binding energy is assumed to be 30 MeV. This momentum distribution is the one which has been successfully used to explain the p+nucleus data.^{25,26}

The calculated momentum spectrum of backward protons in coincidence with forward protons at $\theta = 15^\circ \pm 4^\circ$ agrees well with the spectrum of "p-p QES" with a proper normalization (see Fig.14). The angular distribution is also reproduced well by this model as shown by the dotted line in Fig.16.

On the other hand, the inclusive spectrum calculated by the PWIA is much steeper than that of the experimental data(Fig.7). As stated by Amado et al.², the usual Fermi momentum distribution does not reproduce the inclusive spectrum of backward protons. The reason for the disagreement of the PWIA calculation with the observed inclusive spectrum is obvious now since the inclusive spectrum arises more from the "p-p non-QES" and the "p-p OPC" components than from the "p-p QES" component.

4.3 p-d Quasi-Elastic Scatterings and the Properties of Correlated Clusters

In p-d quasi-elastic scattering, an incident proton is elastically scattered by a deuteron-like two-nucleon system (hereafter called "d") inside the target nucleus. The main reaction mechanism of large momentum transfer is due to a pickup of a neutron from "d" (see Fig. 22). In this section we discuss,

- (1) how does "d"s moves inside the nucleus (P_S distribution), and
- (2) absolute value of the p-d QES cross section and the mean free path of deuterons inside the nucleus.

where P_S is the sum momentum ($P_S = P_n + P_p$) of the neutron momentum (P_n) and the proton momentum (P_p) for "d".

4.3.1 Width of the Sum-Momentum(P_S) Distribution

The use of a plane wave impulse approximation(PWIA) should be appropriate in the present case, since the distorted wave does not strongly affect the spectrum shape²⁷ but only the normalization. In PWIA the differential cross section($\Sigma(\text{pd QES})$) can be written as,

$$\Sigma(\text{pd QES}) = N_d D \int \Sigma(\text{pd el}) \cdot f(P_S) \cdot dP_S, \quad (4.4)$$

where $f(P_S)$ represents a momentum distribution of "d", $\Sigma(\text{pd el})$ is the differential cross section of the p-d elastic scattering, N_d is the total number of "d" inside the nucleus, and D is the attenuation factor due to the loss of particles along the path through which the incident proton, the outgoing deuteron, and the outgoing proton traverse inside the target nucleus. The momentum distribution of "d" inside the nucleus is assumed to be a Gaussian type of the form, $\exp(-P^2/2\sigma_d^2)$. The width, σ_d , as well as the binding energy of "d" to the nucleus, $\text{BE}(\text{"d"})$ were taken as free parameters. The best fit to the data were obtained when $\sigma_d = 85 \pm 15 \text{ MeV/c}$ and $\text{BE}(\text{"d"}) = 60 \text{ MeV}$. The momentum spectrum thus fitted is shown by a dashed curve in Fig. 23. The absolute value of the cross section, which relates to D , will be discussed in the next section.

The present value of σ_d is smaller than the momentum spread observed for deuteron fragments (as projectile fragments) in high-energy heavy-ion reactions, i.e. $\sigma_d = 135 \text{ MeV/c}$ for ^{12}C and ^{16}O projectiles at 2.1 GeV/nucleon of incident energy.^{28,29} In what

follows we consider a possible reason for such a difference. The root-mean-square(rms) momentum of "d" can be expressed as,

$$\langle P_d^2 \rangle^{1/2} = (\langle P_p^2 \rangle + \langle P_n^2 \rangle + 2\langle P_p P_n \rangle)^{1/2} \quad (4.5)$$

For a Gaussian distribution the rms value $\langle P^2 \rangle^{1/2}$ is related to the width σ by $\langle P^2 \rangle^{1/2} = \sqrt{3}\sigma$. Therefore,

$$\sigma_d = (\sigma_p^2 + \sigma_n^2 + 2/3\langle P_p P_n \rangle)^{1/2} \quad (4.6)$$

From the data of ep and pp QES we have $\sigma_p = 100$ MeV/c for ^{12}C nucleus.³⁰ According to a purely statistical calculation, the correlation term is given by³¹ $\langle P_p P_n \rangle = -\langle P_p^2 \rangle / (A-1) = -910$ (MeV/c)². In this case Eq.(4.6) leads to $\sigma_d = 139$ MeV/c which is close to the value obtained by the projectile fragmentation ($\sigma_d = 135$ MeV/c), here σ_n is assumed to be equal to σ_p . In contrast with this, the width observed in p-d QES is much narrower than the above statistical value and it is even smaller than the width of the single particle distribution. Therefore, the "d", which is responsible for p-d QES, does not seem to originate from randomly selected two nucleons. Instead, it seems to originate from pn pairs which have a strong anti-parallel momentum coupling ($\langle P_p P_n \rangle < 0$) since in this case the value of σ_d can be small. The fact that $\langle P_p P_n \rangle < 0$ may further indicate that high momentum protons originate from highly correlated nucleon pairs. The relation between σ_d and the two-particle momentum distribution was reported in Ref.32.

4.3.2 Mass Dependence of the Cross Section

In this section we try to determine the mean free path of the deuteron inside the nucleus and then to calculate the absolute value of the cross section using the mean free path.

Events that fall in the region of p-d QES are those in which the outgoing proton and deuteron are not rescattered inside the target nucleus after the first p-"d" collision. The attenuation of p-d QES depends on the mean free paths of the incident proton (λ_i), the outgoing proton (λ_p), and the deuteron (λ_d). We perform a geometrical calculation similar to that used for p-p QES to obtain the mean free path of the proton inside the

nucleus in a previous report(Ref.26). If we define the path length for three particles by l_i , l_B , and l as shown in Fig. 24, then the attenuation factor(D) can be written as

$$D = \frac{\int e^{-l_i/\lambda_i} \cdot e^{-l_B/\lambda_B} \cdot e^{-l/\lambda_d} \cdot d\vec{r}}{\int d\vec{r}} \quad (4.7)$$

The attenuation of p-p QES, which is measured at the same scattering angles, is obtained by Eq.(4.7) replacing λ_d by λ_p , the mean free path of the forward going protons. The ratio(R) of p-d QES to p-p QES cross section depends, therefore, on the mass of the target only through λ_p and λ_d . The ratios(R) obtained by the present measurement are plotted in Fig.24. The abscissa of the figure is the mean path length $\langle l \rangle$ of the forward going particles defined as,

$$\langle l \rangle = \frac{\int e^{-l_i/\lambda_i} \cdot e^{-l_B/\lambda_B} \cdot l \cdot d\vec{r}}{\int e^{-l_i/\lambda_i} \cdot e^{-l_B/\lambda_B} \cdot d\vec{r}} \quad (4.8)$$

The mean free paths of the incident and the backward protons are assumed to be $\lambda_i = 2.5$ fm and $\lambda_B = 5$ fm. The result was insensitive to the value of the λ_B in the wide range($3 \leq \lambda_B \leq 10$ fm).

The ratio(R) decreases sharply with increasing A , from which we conclude that deuterons (or "d"s) are rescattered more frequently than protons. The data were fitted by a function

$$\exp(-1/\lambda_d - 1/\lambda_p) \cdot \langle l \rangle \quad (4.9)$$

where λ_d and λ_p are the mean free paths of the deuteron in p-d QES and the forward going proton in p-p QES, respectively. Using the mean free path $\lambda_p = 2.5$ fm²⁶, λ_d is estimated to be 1.7 ± 0.3 fm at a deuteron momentum of 1.6 GeV/c. It should be noted that the mean free path of the deuteron as well as that of the proton was not determined by the size of the cross section but by the mass dependence of the cross section.

Using the number of "d" as $2NZ/A$ and the attenuation factor calculated by Eq.(4.7), the calculated momentum integrated cross sections give a reasonable fit to the data as shown by the solid curve in Fig. 19.

5. CONCLUSIONS

We have measured the distribution of protons and deuterons associated with backward energetic protons over a wide kinematical range. The present experiment covers the kinematical region of both p-p and p-d quasi-elastic scatterings as well as quasi-deuteron breakups. We demonstrated that various reaction mechanisms are kinematically separable. We studied the slope factor of the backward proton spectra, the in-plane to out-of-plane ratio, the angular distribution, and the target mass dependence of those different components. Our data showed that p-p quasi-elastic scatterings gives minor contributions to BEP(backward energetic protons). Components of "p-p non-QES" and "p-p OPC", which turn out to be the main components of the BEP, are considered to be mainly from the proton scattering with a correlated nucleon cluster. It is also supported by the associated nucleon multiplicity $\langle m \rangle = 2.4$. Although, the quantitative separation between cluster scattering and multiple scatterings remains for further studies.

The data of p-d quasi-elastic scattering were analyzed with a plane wave impulse approximation. It is found that the momentum spread of the pn system("d") inside the nucleus is smaller than that for deuterons observed in projectile fragments in high-energy heavy-ion collisions. The observed spread(85 ± 15 MeV/c) is also smaller than the width calculated from a purely statistical model. It implies that "d", that is responsible for p-d QES, consists of a pn pair with an anti-parallel momentum coupling between p and n with the coupling stronger than expected from a purely statistical consideration.

From the observed A-dependence of the ratio between p-d QES to p-p QES cross sections, the mean free path of deuterons in the nucleus was estimated to be 1.7 ± 0.3 fm at $P_d = 1.6$ GeV/c. The absolute value and the mass dependence of the p-d QES cross sections are well reproduced by the calculation based on PWIA and the attenuation due to rescattering.

Acknowledgements

The present measurements have been carried out at the Bevatron/ Bevalac at the Lawrence Berkeley Laboratory. We acknowledge with thanks the important help by the Bevatron crews. Our special thanks go to R. Fuzesy for his technical support for the

preparation of the experiment. Fruitful discussions with J. Knoll, J. Randrup, M. Sano, H. Sato, and H. Tezuka, are gratefully acknowledged. This work was supported by the Director, Division of Nuclear Physics of the Office of High Energy and Nuclear Physics of the US Department of Energy under Contract DE-AC03-76SF00098, the INS-LBL Collaboration Program, and by the U.S.-Japan Joint Program.

REFERENCES

- a) Permanent address: Department of Physics, Faculty of Science, University of Tokyo, Hongo, Bunkyo-ku, Tokyo 113, JAPAN.
 - b) Present address: Serin Physics Laboratory, Rutgers University, Piscataway, NJ. 08854, USA.
 - c) Also, Department of Physics, University of California, Berkeley, Ca. 94720, USA.
1. S. Frankel, W. Frati, O. Van Dyck, R. Werbeck, and V. Highland, Physical Review Letters 36, 642 (1976).
 2. R. D. Amado, and R. M. Woloshyn, Physical Review Letters 36, 1435 (1976).
 3. S. Frankel, Phys. Rev. Letters 38, 1338 (1976).
 4. S. Frankel, Phys. Rev.C 17, 694 (1978).
 5. S. Frankel, W. Frati, G. Blanpied, G. W. Hoffmann, T. Kozlowski, C. Morris, H. A. Thiessen, O. Van Dyck, R. Ridge, and C. Whitten, Phys. Rev.C 18, 1375 (1978).
 6. S. Frankel, W. Frati, R. M. Woloshyn, and D. Yang, Phys. Rev.C 18, 1378 (1978).
 7. C. F. Perdrisat, S. Frankel, and W. Frati, Phys. Rev.C 18, 1764 (1978).
 8. Y. D. Bayukov, V. I. Efremenko, S. Frankel, W. Frati, M. Gazzaly, G. A. Leksin, N. A. Nikiforov, C. F. Perdrisat, V. I. Tchistilin, and Y. M. Zaitsev, Phys. Rev.C 20, 764 (1979).
 9. S. Frankel, W. Frati, M. Gazzaly, Y. D. Bayukov, V. I. Efremenko, G. A. Leskin, N. A. Nikiforov, V. I. Tchistilin, Y. M. Zaitsev, and C. F. Perdrisat, Phys. Rev.C 20, 2257 (1979).
 10. S. A. Gurvitz, Phys. Rev. Letters, 47, 560 (1981).
 11. T. Fujita, Phys. Rev. Letters, 39, 174 (1977).
 12. T. Fujita, and J. Hufner, Nucl. Phys. A314, 317 (1979).
 13. T. Fujita, Nucl. Phys. A324, 409 (1979).
 14. T. Yukawa, and S. Furui, Phys. Rev.C 20, 2316 (1979).

15. A. M. Baldin, AIP Conference Proceedings 26 , 621 (1975) and references therein.
16. J. Knoll, Phys. Rev.C 20 , 773 (1979).
17. S. Frankel and R. M. Woloshyn, Phys. Rev.C 16 , 1680 (1977).
18. S. Frankel, W. Frati, M. Gazzaly, G. W. Hoffman, O. Van Dyck, and R. M. Woloshyn, Phys. Rev. Letters 41 , 148 (1978).
19. V. I. Komarov, G. E. Kosarev, H. Muller, D. Netzband, and T. Stiehler, Phys. Letters 69B , 37 (1977).
20. V. I. Komarov, G. E. Kosarev, H. Muller, D. Netzband, T. Stiehler, and S. Tesch, Phys. Letters 80B , 30 (1978).
21. V. I. Komarov, G. E. Kosarev, H. Muller, D. Netzband, V. D. Toneev, T. Stielhler, S. Tesch, K. K. Gudima, and S. G. Mashnik, Nucl. Phys. A326 , 297 (1979).
22. S. Frankel, W. Frati, C. F. Perdrisat, and O. B. Van Dyck, Phys. Rev.C 24 , 2684 (1981).
23. R. E. L. Green, D. H. Boal, R. Helmer, K. P. Jackson, and R. G. Korteling, Nucl. Phys. A405 , 463 (1983).
24. S. Nagamiya, M. C. Lemaire, E. Moeller, S. Schnetzer, G. Shapiro, H. Steiner, and I. Tanihata, Phys. Rev.C 24 , 971 (1981).
25. J. Knoll and J. Randrup, Phys. Letters 103B , 264 (1981).
26. I. Tanihata, S. Nagamiya, S. Schnetzer, and H. Steiner, Phys. Letters 100B , 121 (1981).
27. D. F. Jackson and B. K. Jain, Phys. Letters 27B , 147 (1968).
28. D. E. Greiner, P. J. Lindstrom, H. H. Heckmann, B. Cork, and F. S. Bieser, Phys. Rev. Letters 35 , 152 (1974).
29. L. Anderson, W. Bruckner, E. Moeller, S. Nagamiya, S. Nissen-Meyer, L. Schroeder, G. Shapiro, and H. Steiner, Phys. Rev.C 28 , 1224 (1983).
30. E. J. Moniz, I. Sick, R. R. Whitney, J. R. Ficenece, R. D. Kephart, and W. P. Trower, Phys. Rev. Letters 26 , 445 (1971).

31. A. S. Goldhaber, Phys. Letters 53B, 306 (1974).
32. I. Tanihata, Proceedings of the 1983 INS International Symposium on High Energy Photo-Nuclear Reactions and Related Topics, Sep. 1983 Tokyo, JAPAN, p215.

Table-1 Performance of the detectors

	Magnetic Spectrometer	ΔE -E Telescope
particles	$\pi, p, d, t, {}^3\text{He}$	π, p, d
momentum range (MeV/c)	480-2000	330-700
momentum resolution (typical)	7%	9%
solid angle (msr)	12	29×5
covered angle	$15^\circ - 100^\circ$ ($\Delta\vartheta = 8^\circ$)	$105^\circ - 155^\circ$

Table-2 Momentum resolution of the magnetic spectrometer

momentum P (MeV/c)	resolution $\Delta P/P$ (%)
500	9.0
750	6.0
1000	8.5
1250	11.0

Table-3 Conditions of the Measurements

• Inclusive Cross Section of the Proton ($p + A \rightarrow p + X$)

ϑ : $108^\circ, 118^\circ, 128^\circ, 138^\circ, 148^\circ$
 p : $330 - 700 \text{ MeV}/c$

• Two-Particle Coincidence

p-p coincidence ($p + A \rightarrow p + p + X$) and
 p-d coincidence ($p + A \rightarrow p + d + X$)

ϑ_1 (p or d) : $15^\circ, 20^\circ, 30^\circ, 40^\circ, 55^\circ, 70^\circ, 90^\circ, 100^\circ$
 P_1 (p or d) : $480 - 2000 \text{ MeV}/c$

ϑ_2 (p) : 118°
 P_2 (p) : $330-700 \text{ MeV}/c$

$\Delta\varphi = \varphi_1 - \varphi_2$: 180° (inplane) and 90° (out-of-plane)

Table-4 Slope factors (P_0) of backward proton spectra
in p + KCl reactions*

(P_0 in MeV/c)

coincidence*					
ϑ_1	p-p QES	p-p non-QES	p-p OPC	p-d non-QES	p-d OPC
(degree)	(MeV/c)	(MeV/c)	(MeV/c)	(MeV/c)	(MeV/c)
15	55 ± 5	91 ± 6	68 ± 6	94 ± 8	73 ± 7
20	52 ± 7	81 ± 8	62 ± 7	90 ± 10	83 ± 15
30	--	87 ± 6	57 ± 10	92 ± 10	74 ± 10
40	--	83 ± 8	61 ± 5	89 ± 9	55 ± 7
55	--	87 ± 8	70 ± 7	--	--
70	--	70 ± 10	53 ± 15	--	--
90	--	76 ± 10	57 ± 15	--	--
100	--	70 ± 9	--	--	--
inclusive at 118° 87 ± 2 (MeV/c)					

*coincidence events between a backward proton at $\vartheta_2 = 118^\circ$ and a forward particle (p or d) at various angles ϑ_1 .

Table-5 Slope factors of (P_0) of backward proton spectra^{*1}

(800 MeV p + A)

Target	C	KCl	Pb
	P_0 in MeV/c		
inclusive	88 ± 1	87 ± 2	85 ± 2
p-p QES	56 ± 4	55 ± 3	56 ± 4
p-p non-QES	85 ± 5	91 ± 5	92 ± 4
p-p OPC	72 ± 5	71 ± 3	80 ± 4
p-d QES	(non-exponential shape)		
p-d non-QES	-- ^{*2}	94 ± 8	84 ± 9
p-d OPC	-- ^{*2}	73 ± 7	77 ± 8

^{*1} Coincidence events between a backward proton at $\vartheta_2 = 118^\circ$ and a forward particle (p or d) at $\vartheta_1 = 15^\circ$.

^{*2} Present statistics are too poor to be fitted.

Table-6(a) Two-particle coincidence cross sections

800 MeV p + KCl

 $d^2\sigma/d\Omega_1 d\Omega_2$ at $\vartheta_2=118^\circ$

$\vartheta_1 =$	15°	20°	30°	40° (mb/sr ²)	55°	70°	90°	100°
p-p QES	.49 ±.03	.26 ±.03	.067 ±.012	.010 ±.003	.000 ±.002	.000 ±.001	.000 ±.001	.000 ±.001
p-p non-QES	2.74 ±.08	2.36 ±.09	1.87 ±.06	1.09 ±.03	.60 ±.03	.28 ±.02	.08 ±.01	.040 ±.005
p-p OPC	1.75 ±.08	1.33 ±.08	1.10 ±.05	.64 ±.03	.30 ±.03	.16 ±.02	.07 ±.01	.026 ±.004
p-d QES	.27 ±.03	.06 ±.02	.006 ±.004	.001 ±.001	.000 ±.002	.000 ±.01	.000 ±.001	.000 ±.001
p-d non-QES	.71 ±.04	.49 ±.04	.42 ±.03	.20 ±.01	.10 ±.01	.08 ±.01	.024 ±.006	.007 ±.002
p-d OPC	.40 ±.03	.21 ±.04	.29 ±.03	.15 ±.01	.06 ±.01	.032 ±.008	.020 ±.006	.006 ±.002

Table-6(b) Two-particle coincidence cross sections

800 MeV p + Nucleus

 $d^2\sigma/d\Omega_1 d\Omega_2$ at $\vartheta_1=15^\circ$ and $\vartheta_2=118^\circ$

Target	C	NaF	KCl	Ag (mb/sr ²)	Pb
p-p QES	.24 ± .02	.21 ± .03	.49 ± .03	.62 ± .07	.99 ± .13
p-p non-QES	.98 ± .05	1.43 ± .07	2.74 ± .08	4.42 ± .19	5.10 ± .29
p-p out-of-plane	.57 ± .04	.95 ± .07	1.89 ± .08	3.55 ± .18	4.98 ± .32
p-d QES	.19 ± .03	.18 ± .03	.27 ± .03	.22 ± .05	.33 ± .09
p-d non-QES	.23 ± .02	.34 ± .03	.71 ± .04	1.30 ± .10	1.18 ± .13
p-d out-of-plane	.10 ± .02	.20 ± .03	.40 ± .03	.70 ± .08	1.17 ± .16

Table-7 Integrated cross sections (σ_I)*

(800 MeV p + KCl)

	σ_I (mb/rad·sr)
p-p QES	0.05
p-p non-QES	0.80
p-p OPC	0.47
p-d QES	0.03
p-d non-QES	0.16
p-d OPC	0.11

$$*\sigma_I = \int_0^\pi d^2\sigma / d\Omega_1 d\Omega_2 \cdot \sin\vartheta_1 \cdot d\vartheta_1$$

Table-8 Observations in pA collisions ($\theta_p(\text{back}) = 118^\circ$)

	inclusive	p + A \rightarrow p + p + X			p+A \rightarrow p + d + X			
		QES	non-QES	OPC	QES	non-QES	OPC	
(P_0 in MeV/c) • Slope factor	87 \pm 2	55 \pm 5	91 \pm 6	68 \pm 6	--	94 \pm 8	73 \pm 7	$\frac{d\sigma}{dpd\Omega} \propto e^{-P/P_0}$, A = KCl, $\theta_1 = 15^\circ$ very small dependence on A and angle
• Cross sections σ_I (in mb/rad.Sr)		0.05	0.80	0.47	0.03	0.16	0.11	A = KCl
• Angular dependence		very sharp	slow	slow	sharp	slow	slow	A = KCl, independent of A
• A-dependence α in (A^α)	1.0	~ 0.55	~ 0.7	~ 0.8	~ 0.2	~ 0.7	~ 0.8	$\theta_1 = 15 \sim 40^\circ$; A-dependence is stronger for $\theta_1 > 70^\circ$
• $\langle m \rangle$	3.3 (6.2mb/Sr)	2.4						associated multiplicity for coincidence measurement; A = KCl

FIGURE CAPTIONS

Fig. 1. The momentum region covered by the present experiment is shown by a hatched rectangular. The horizontal axis is the momentum of the forward proton at $\theta=15^\circ$ and the vertical axis is the momentum of the backward proton at $\theta=118^\circ$. Solid lines show kinematical relations between forward and backward protons produced by the elastic scattering of the incident proton with protons and nucleon clusters which have Fermi motion inside the target nucleus. Numbers beside the curves indicate the momentum of the proton (or clusters) inside the target nucleus. Because the breakups of clusters are responsible for two-proton coincidence measurement, curves for p-d, p-t, p- α are drawn as a function of the momentum per nucleon. Therefore these curves are the kinematical loci of the gentle (small relative momentum) breakup reactions. The kinematical locus of large relative momentum breakup of p-(2N) reaction with no Fermi motion is also shown by a dotted curve. The dotted rectangle shows the momentum range covered by the measurement in refs.20,21.

Fig. 2. Schematic view of the counter setup. Two sets of $\Delta E-E$ counters (RB and UB) covered $\theta=105^\circ - 155^\circ$ at $\phi=90^\circ$ and 180° . The magnetic spectrometer covered 8° in θ at $\phi=0^\circ$ and was rotated from 15° to 100° in θ .

Fig. 3. Plan view of the $\Delta E-E$ counter. (a) The first ΔE -counter (RB1), (b) The second ΔE -counter (RB2), (c) E -counters (RB3), and (d) a veto counter. All the counters are made of plastic scintillators.

Fig. 4. A typical scatter plot between E and ΔE . A clear separation between pion, proton, and deuteron is seen.

Fig. 5. Energy calibration curve of a $\Delta E-E$ counter. The calibration was done by the TOF counter. The energy E_{\min} and E_{\max} written in the figure indicate the minimum and the maximum energies of the $\Delta E-E$ counter calculated by the range-energy relation.

Fig. 6. An effective solid angle of a E -counter as a function of the proton momentum. The change of the solid angle is due to the multiple scattering in the first and second scintillators. A solid line in the figure shows the solid angle used for the present

analysis. A dashed line shows the geometrical solid angle.

Fig. 7. Inclusive momentum spectra of protons at $\theta=118^\circ$ in 800 MeV p+Pb, p+KCl, and p+C collisions. Error bars in the figure show the statistical errors. The systematic error is estimated to be less than 20%. A dotted curve shows the result of a PWIA calculations (see discussion in sec. 4.2).

Fig. 8. Angular distributions of the inclusive protons. The cross sections are obtained by integration over the momentum range from 350 to 700 MeV/c. Statistical errors are smaller than the size of the plotted circles unless indicated. A systematic error is estimated to be less than 20%.

Fig. 9. Target mass dependence of the inclusive proton cross section. Error bars show only statistical errors.

Fig. 10. Momentum-momentum scatter plots of two-proton events for in-plane coincidence (a) and for out-of-plane coincidence(b). One unit in the figure corresponds to $2.07 \text{ nb}/(\text{sr.MeV/c})^2$. See text for further information.

Fig. 11. Momentum-momentum scatter plots of proton-deuteron coincidence events. The mark "+" shows the kinematics of the p-d elastic scattering.

Fig. 12. Distribution of the excitation energy(E_{ex}) of the residual nucleus for p-p events. Statistical errors are not shown for out-of-plane data but they have similar amount of errors as in-plane data. A peak near $E_{ex}=0$ shows the contribution from p-p quasi-elastic scatterings. Another peak at $E_{ex}\approx 450 \text{ MeV}$ is due to the instrumental kinematical limit.

Fig. 13. Distributions of E_{ex} for p-d events. A clear peak correspond to p-d QES is seen.

Fig. 14. Spectra of the backward protons for the different components in p+KCl collisions. Solid lines are the exponential fit to the data. Error bars in the figure show only statistical errors. A dotted curve shows the result of a PWIA calculations (see discussion in sec. 4.2).

Fig. 15. Spectra of the backward protons for the different components of p-d events. Solid lines are the exponential fit to the data. Error bars in the figure show only statistical errors.

Fig. 16. Angular distributions of protons in coincidence with backward protons at $\theta_2=118^\circ$. Error bars are only for statistical errors. A dotted curve shows the result of a PWIA calculations (see sec. 4.2).

Fig. 17. Angular distributions of deuterons in coincidence with backward($\theta=118^\circ$) protons. Error bars are only for statistical errors.

Fig. 18. Mass number dependence of the p-p coincidence cross section. Error shown are only for statistical errors.

Fig. 19. Target mass number dependences of the p-d coincidence cross sections. Error shown are only for statistical errors. A solid curve shows the result of the PWIA model calculation described in section 4.2.

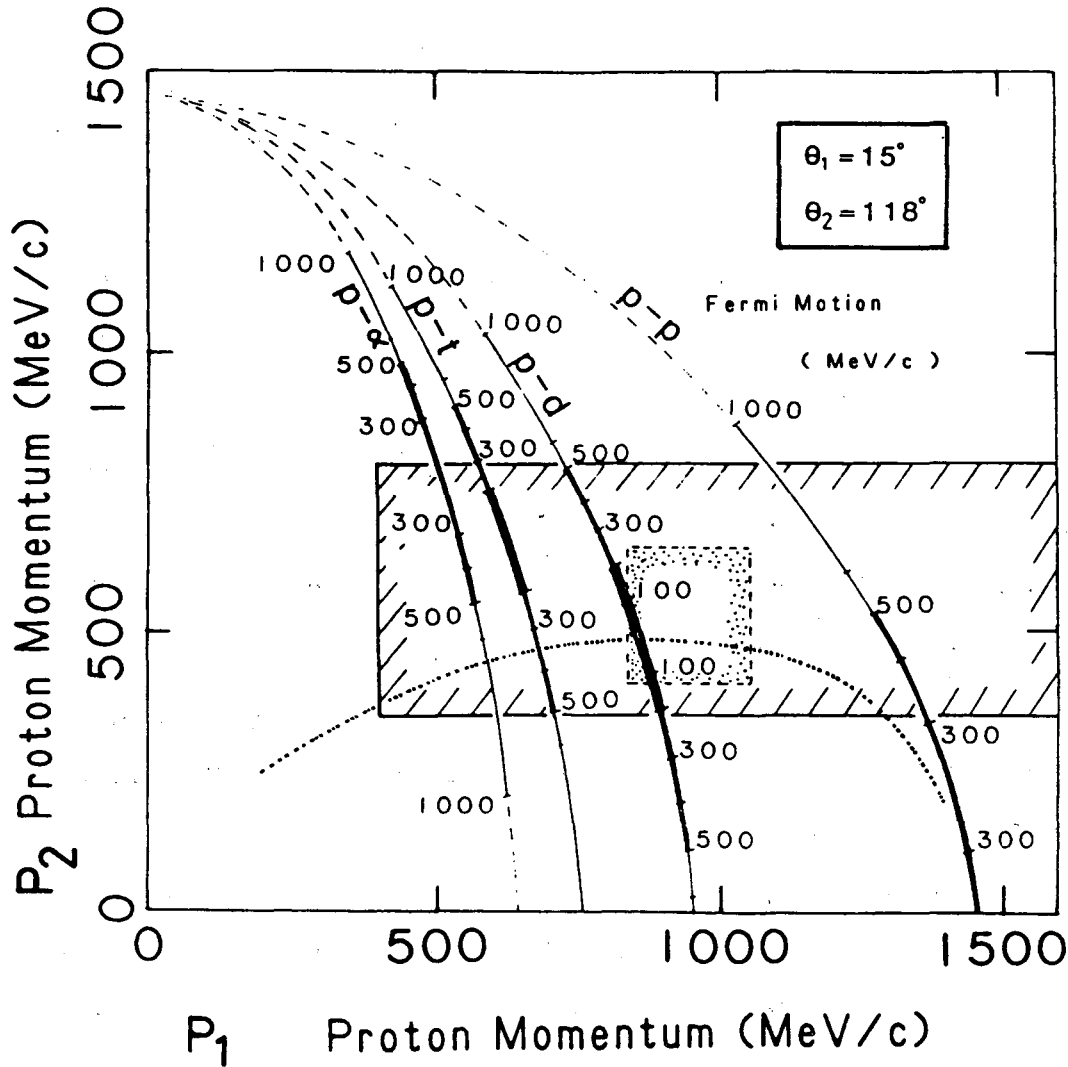
Fig. 20. A backward proton spectrum of the "p-d QES" (solid circles) events and a difference spectrum between "p-p non-QES" and "p-p OPC" in the collision of p+KCl at the angles $\theta_1(=\theta_d)=15^\circ$ and $\theta_2=118^\circ$. Only statistical errors are shown in the figure.

Fig. 21. Contour line plot of the difference ("p-p in-plane" - "p-p OPC") of the double differential cross section. Kinematical loci of p-p QES and p-(2N) breakup reactions are also shown. A broad concentration of the events are seen around the p-(2N) breakup region.

Fig. 22. The reaction mechanism of p-d QES at large momentum transfer. Incident proton picks up a neutron which have a momentum ($K_d - K_p$). The proton which was correlated with the neutron is emitted at a large angle.

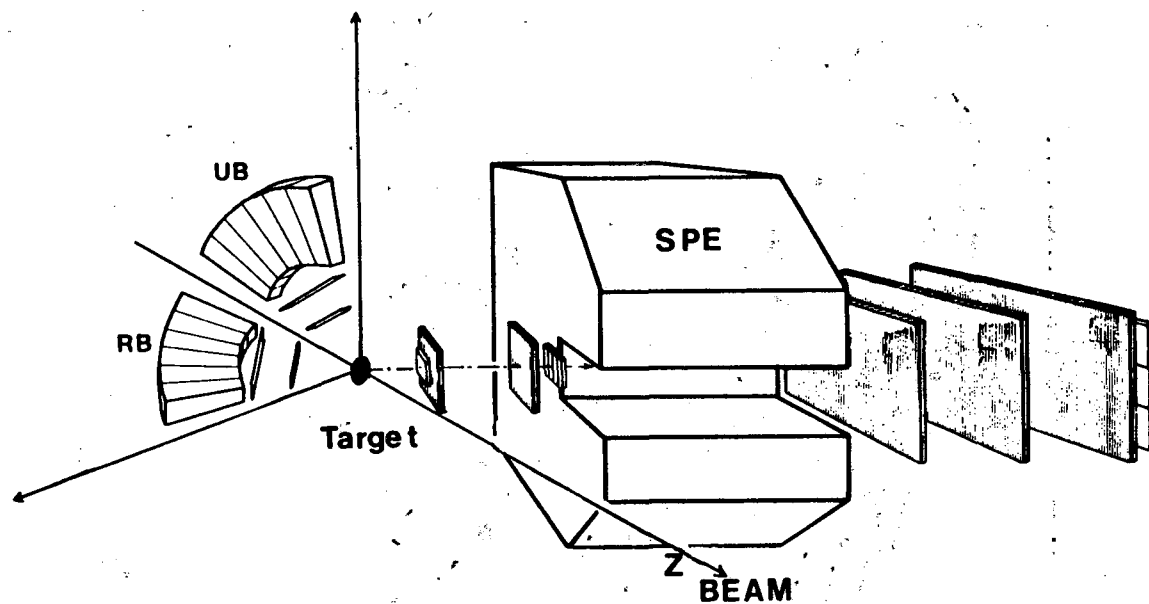
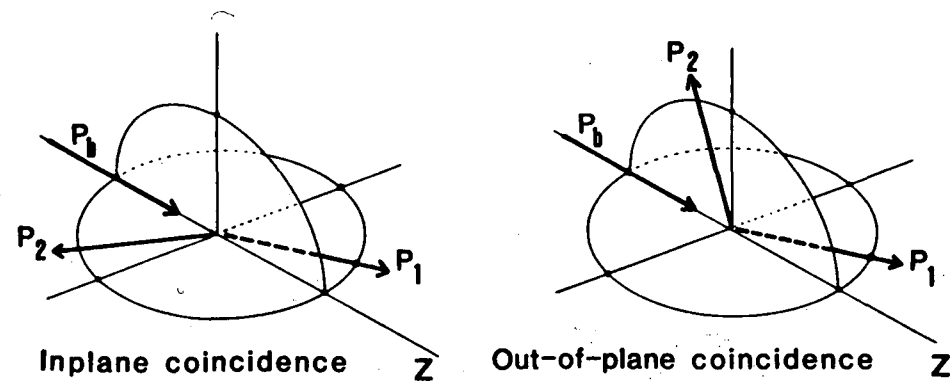
Fig. 23. Momentum spectra of backward protons associated with "p-d QES". A dashed curve shows the spectrum fitted to the data by a PWIA calculations. The momentum expected from p-d elastic scatterings are indicated by the arrow.

Fig. 24. The cross section ratio(R) between p-d to p-p QES plotted as a function of the effective path length $\langle l \rangle$ of forward deuterons.



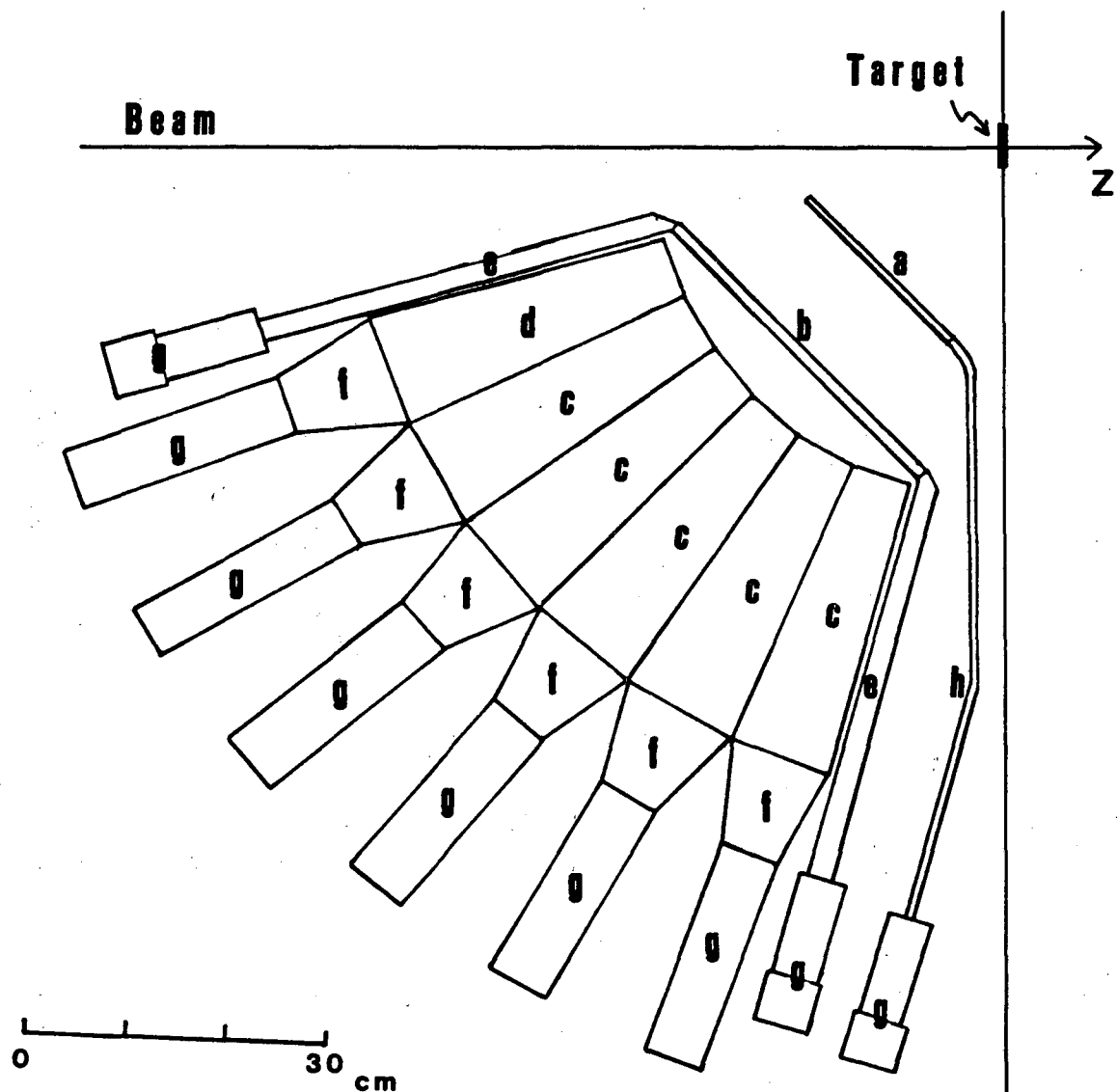
XBL 843-1116

Fig. 1. The momentum region covered by the present experiment is shown by a hatched rectangular. The horizontal axis is the momentum of the forward proton at $\theta=15^\circ$ and the vertical axis is the momentum of the backward proton at $\theta=118^\circ$. Solid lines show kinematical relations between forward and backward protons produced by the elastic scattering of the incident proton with protons and nucleon clusters which have Fermi motion inside the target nucleus. Numbers beside the curves indicate the momentum of the proton (or clusters) inside the target nucleus. Because the breakups of clusters are responsible for two-proton coincidence measurement, curves for p-d, p-t, p- α are drawn as a function of the momentum per nucleon. Therefore these curves are the kinematical loci of the gentle (small relative momentum) breakup reactions. The kinematical locus of large relative momentum breakup of p-(2N) reaction with no Fermi motion is also shown by a dotted curve. The dotted rectangle shows the momentum range covered by the measurement in refs. 20, 21.



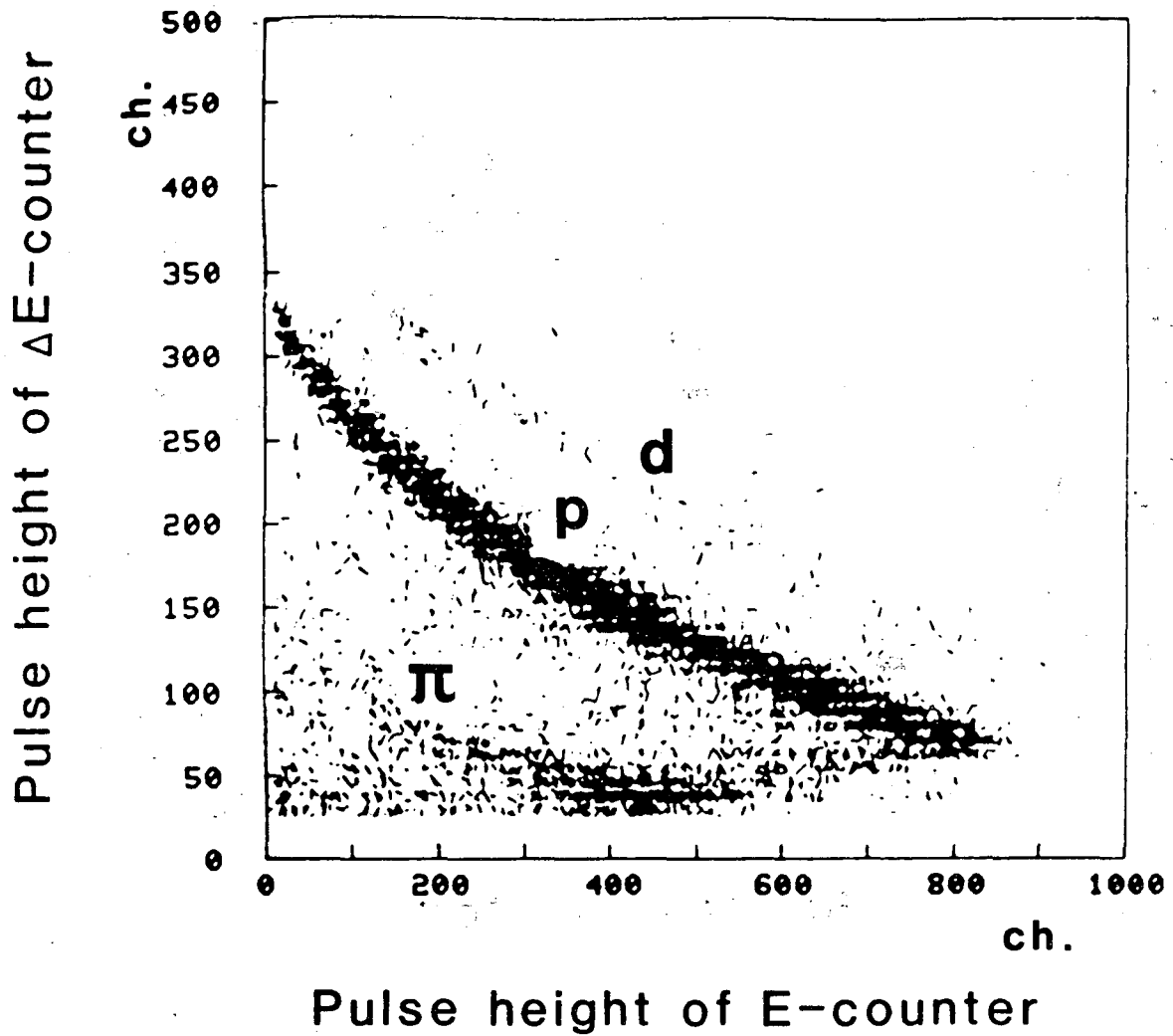
XBL 843-1117

Fig. 2. Schematic view of the counter setup. Two sets of $\Delta E-E$ counters (RB and UB) covered $\theta=105^\circ - 155^\circ$ at $\phi=90^\circ$ and 180° . The magnetic spectrometer covered 8° in θ at $\phi=0^\circ$ and was rotated from 15° to 100° in θ .



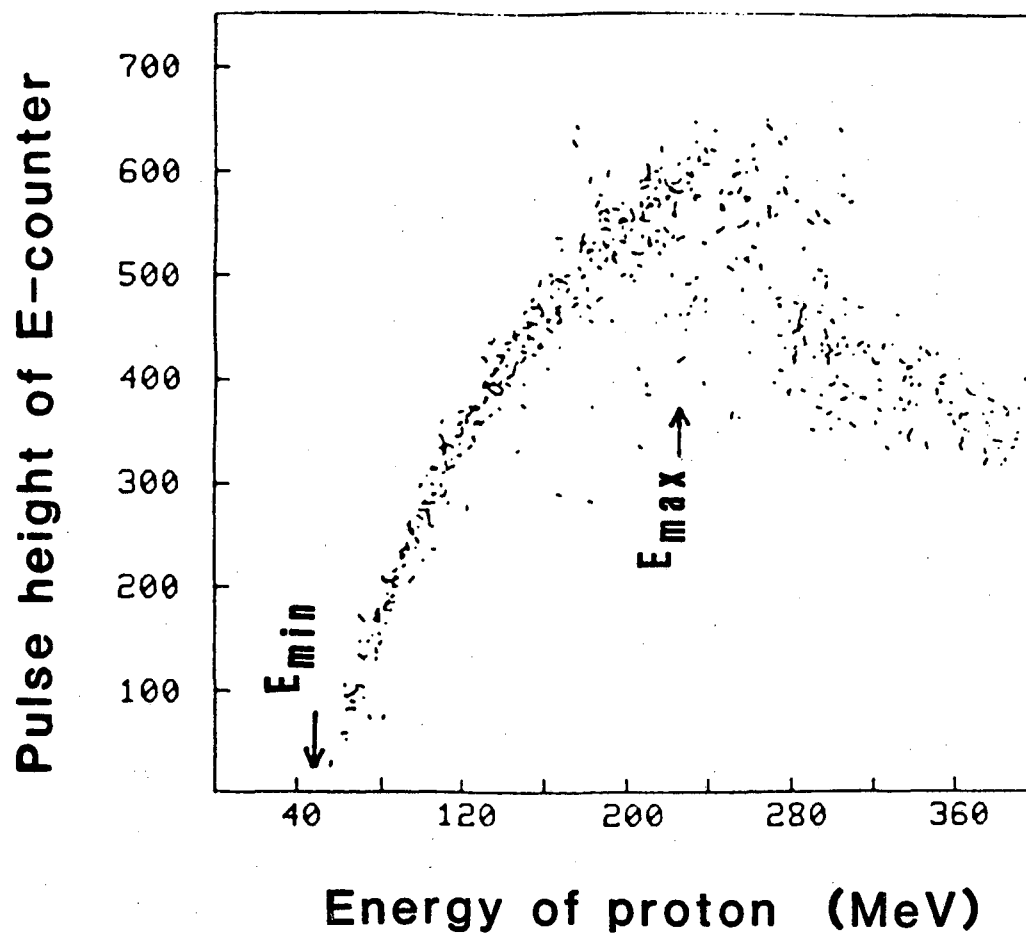
XBL 843-1118

Fig. 3. Plan view of the ΔE - E counter. (a) The first ΔE -counter(RB1), (b) The second ΔE -counter(RB2), (c) E -counters(RB3), and (d) a veto counter. All the counters are made of plastic scintillators.



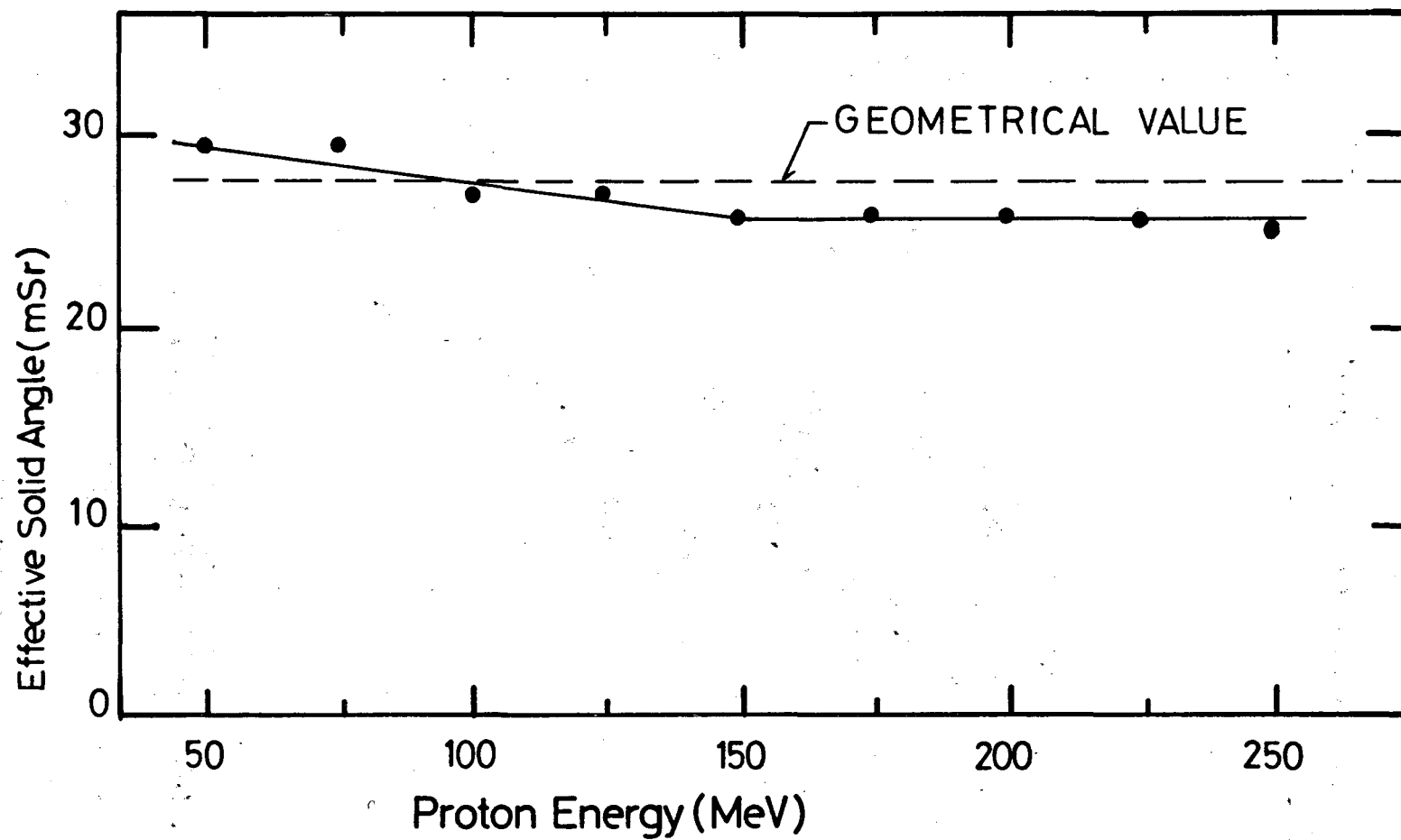
XBL 843-1120

Fig. 4. A typical scatter plot between E and ΔE . A clear separation between pion, proton, and deuteron is seen.



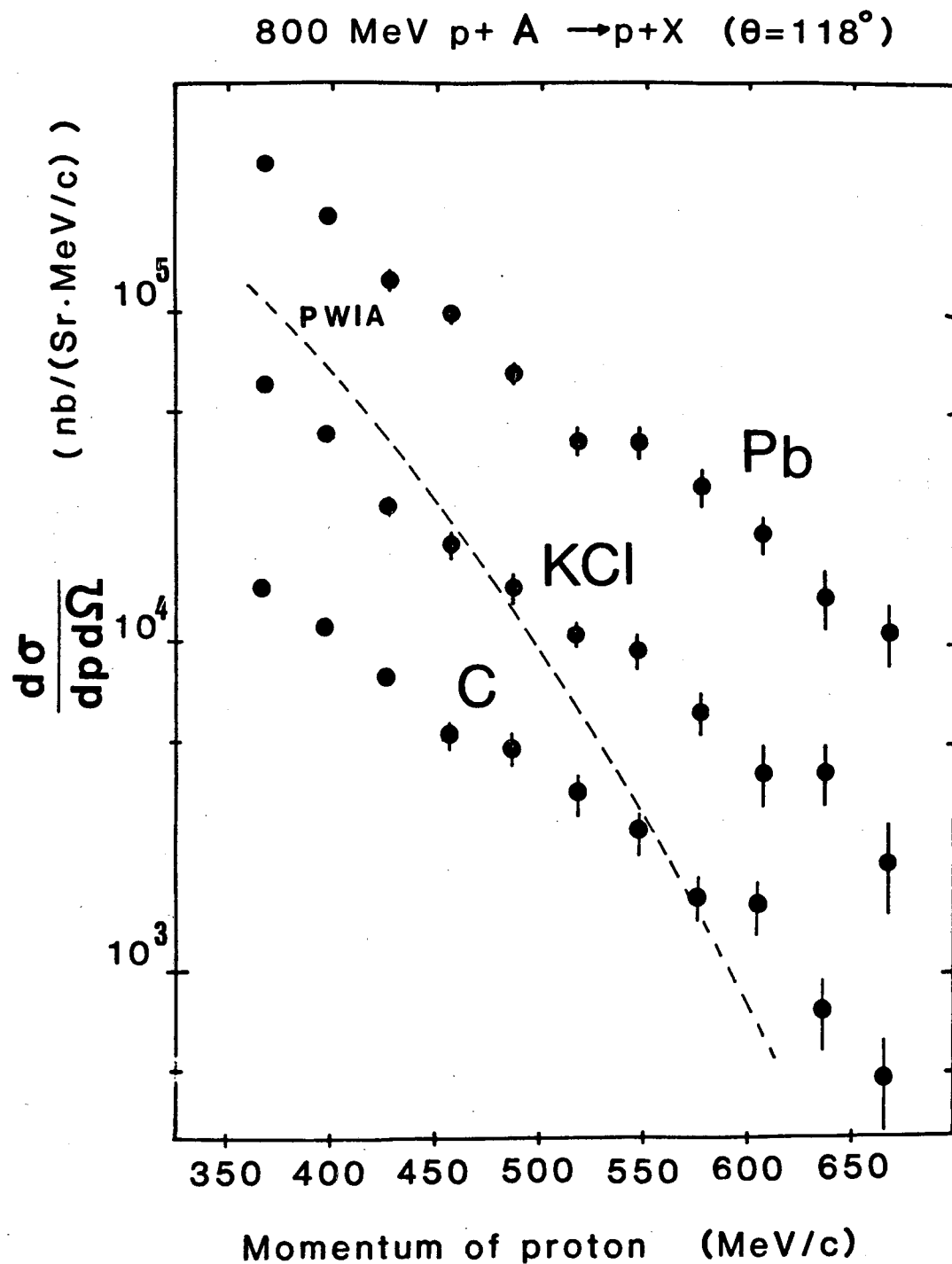
XBL 843-1119

Fig. 5. Energy calibration curve of a $\Delta E-E$ counter. The calibration was done by the TOF counter. The energy E_{min} and E_{max} written in the figure indicate the minimum and the maximum energies of the $\Delta E-E$ counter calculated by the range-energy relation.



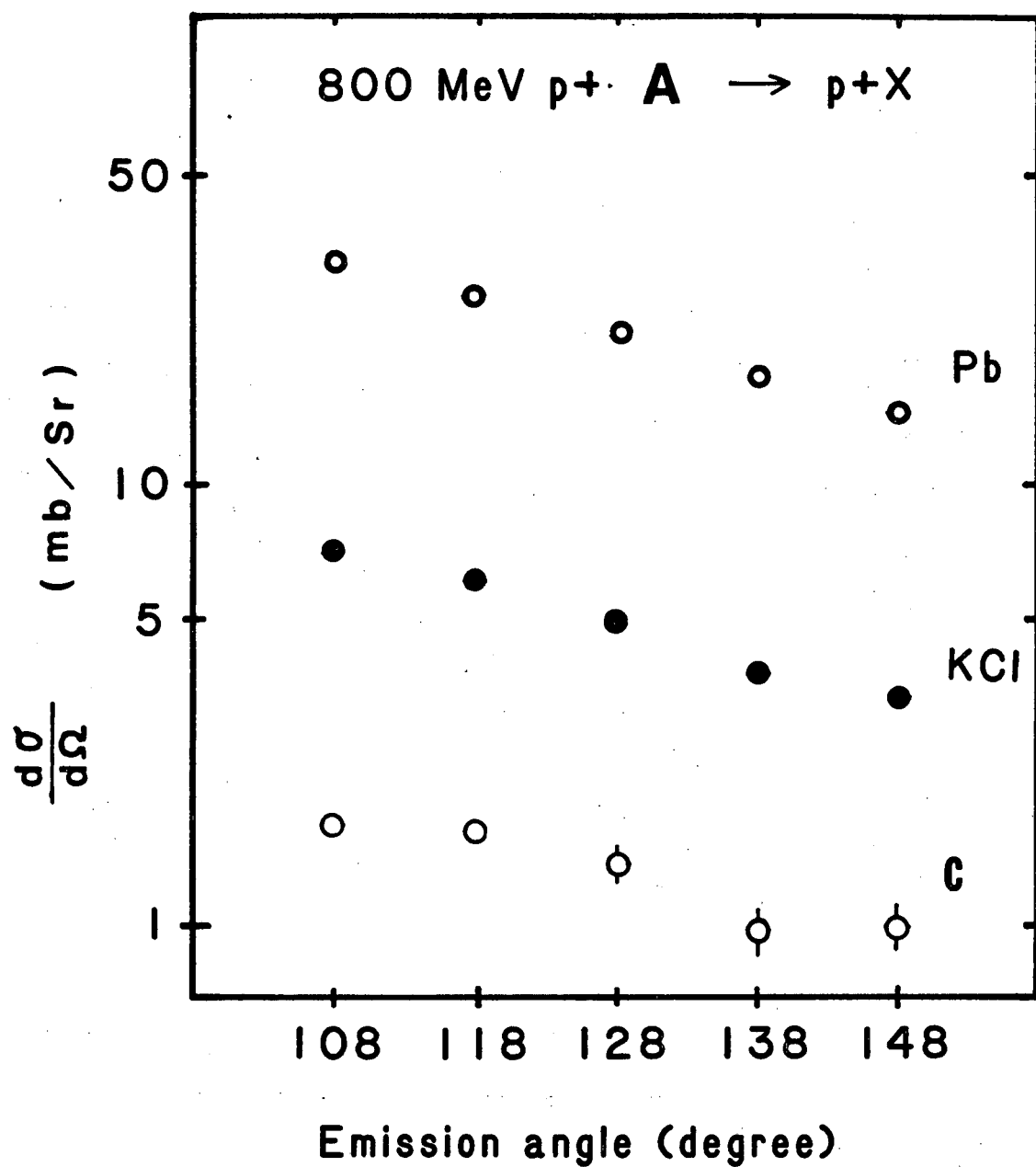
XBL 843-1121

Fig. 6. An effective solid angle of a E-counter as a function of the proton momentum. The change of the solid angle is due to the multiple scattering in the first and second scintillators. A solid line in the figure shows the solid angle used for the present analysis. A dashed line shows the geometrical solid angle.



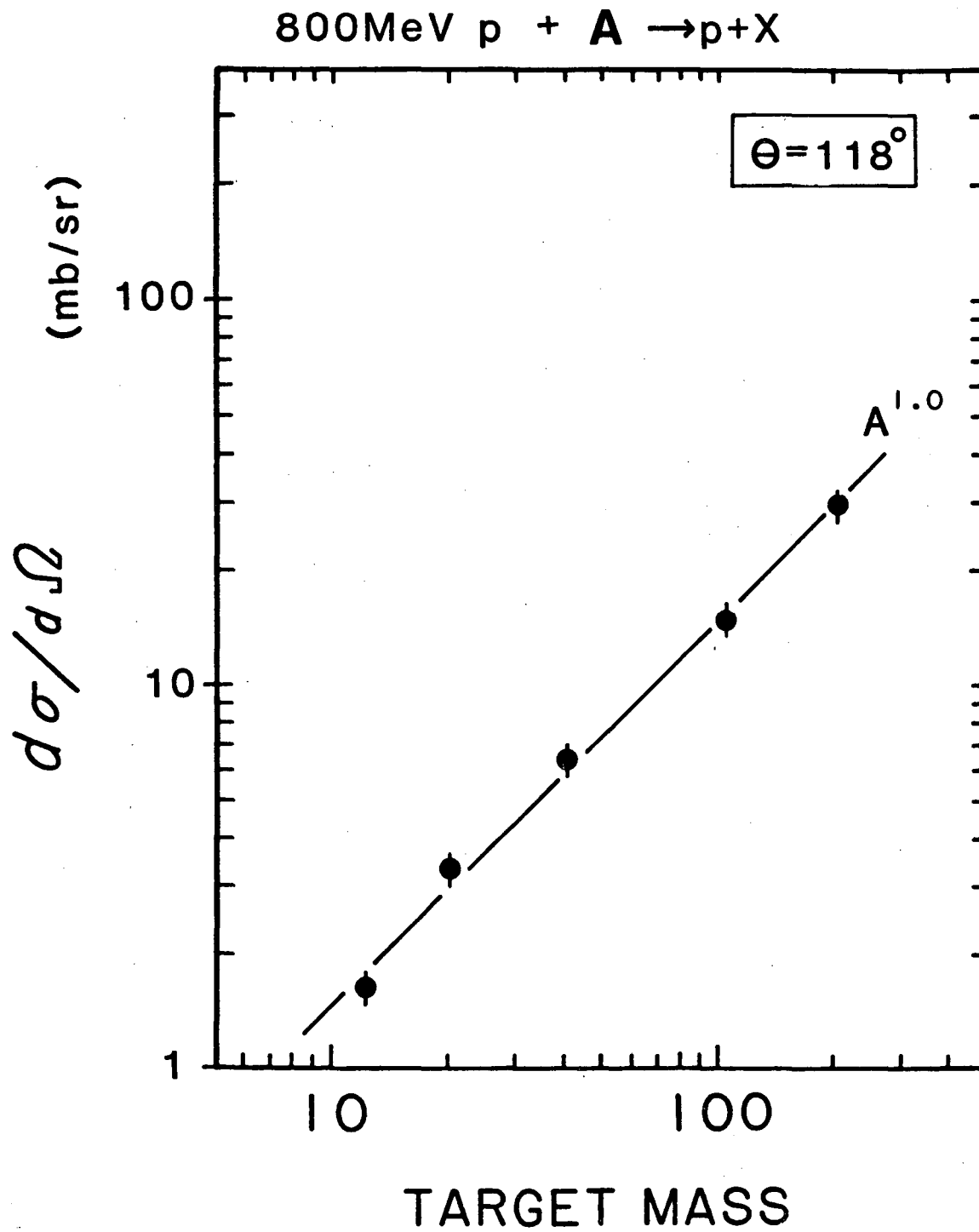
XBL 843-1122

Fig. 7. Inclusive momentum spectra of protons at $\theta = 118^\circ$ in 800 MeV p+Pb, p+KCl, and p+C collisions. Error bars in the figure show the statistical errors. The systematic error is estimated to be less than 20%. A dotted curve shows the result of a PWIA calculations (see discussion in sec. 4.2).



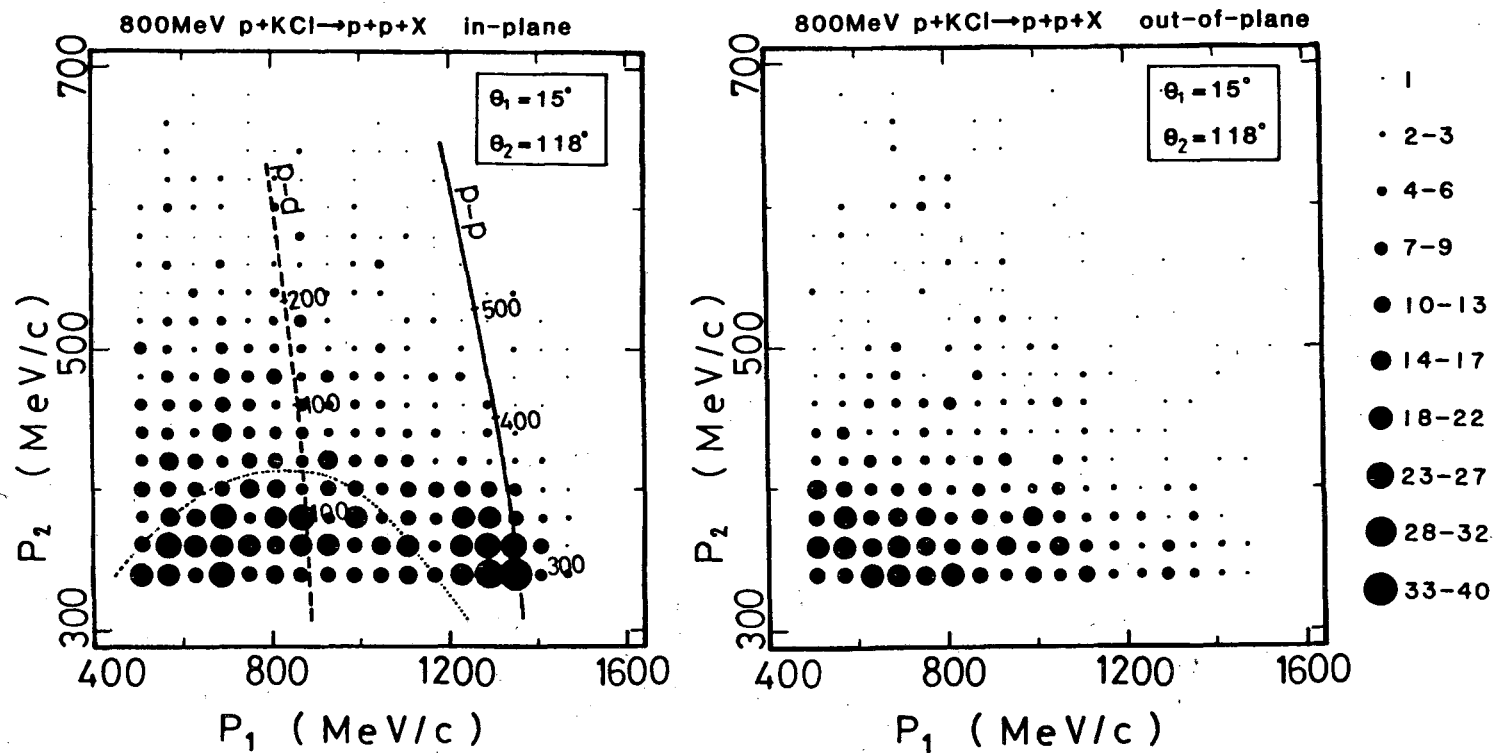
XBL 843-1123

Fig. 8. Angular distributions of the inclusive protons. The cross sections are obtained by integration over the momentum range from 350 to 700 MeV/c. Statistical errors are smaller than the size of the plotted circles unless indicated. A systematic error is estimated to be less than 20%.



XBL 843-1124

Fig. 9. Target mass dependence of the inclusive proton cross section. Error bars show only statistical errors.



XBL 843-1125

Fig. 10. Momentum-momentum scatter plots of two-proton events for in-plane coincidence (a) and for out-of-plane coincidence (b). One unit in the figure corresponds to $2.07 \text{ nb}/(\text{sr} \cdot \text{MeV}/c)^2$. See text for further information.

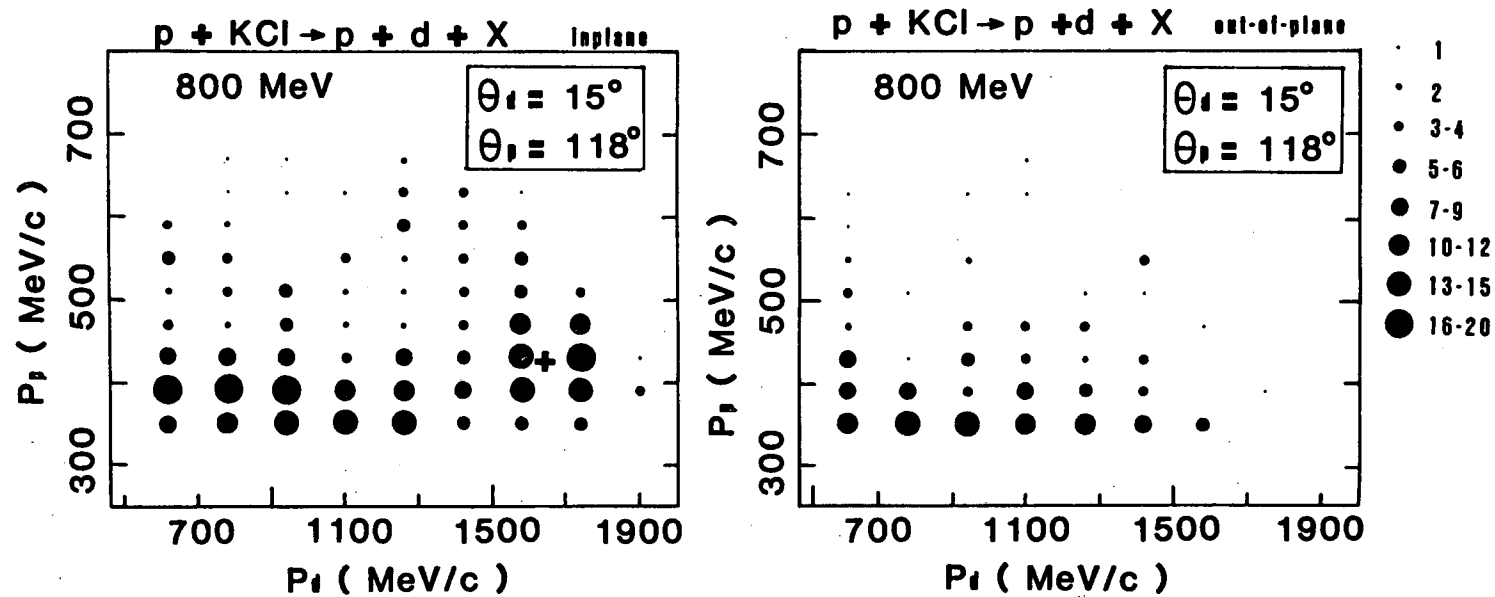
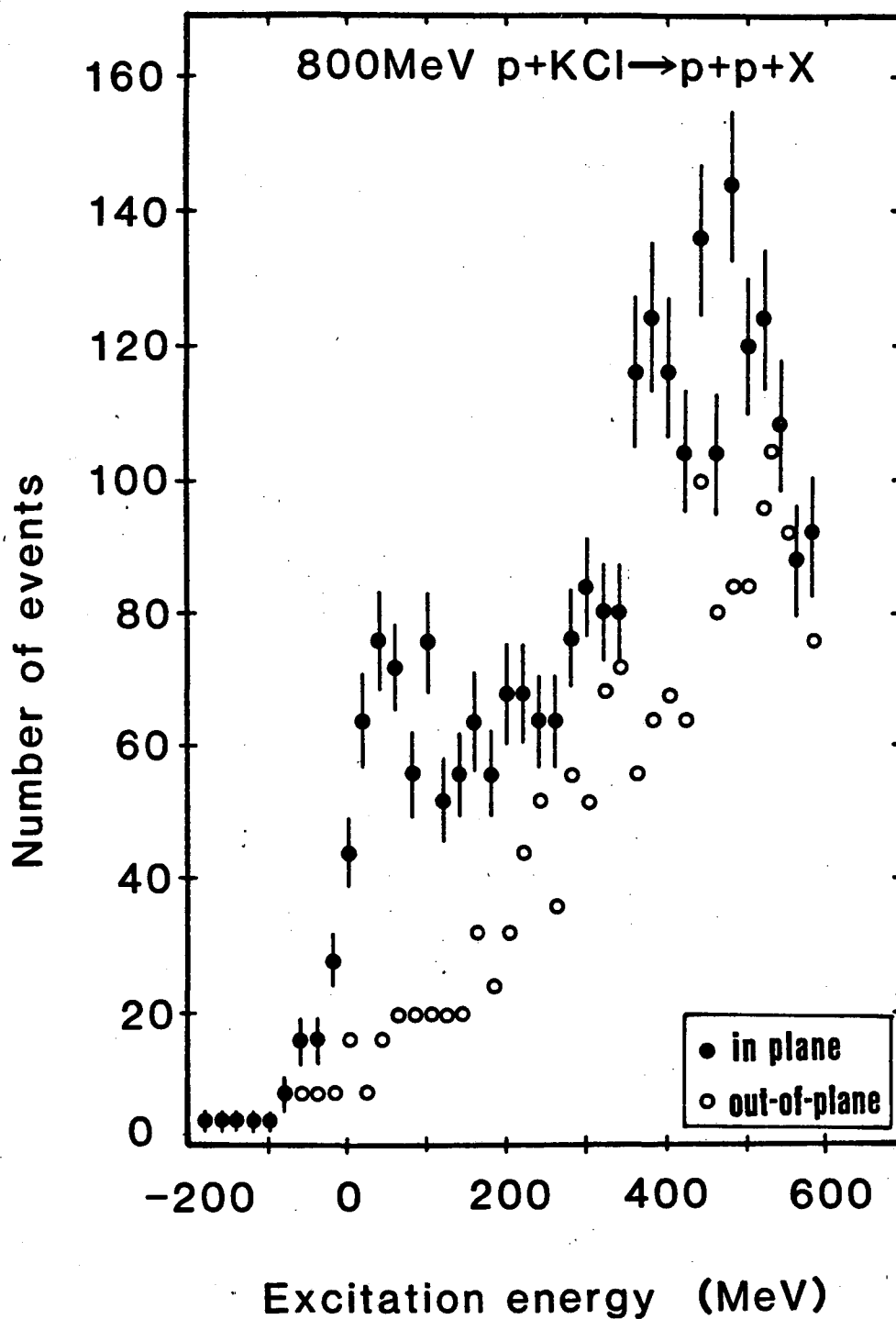


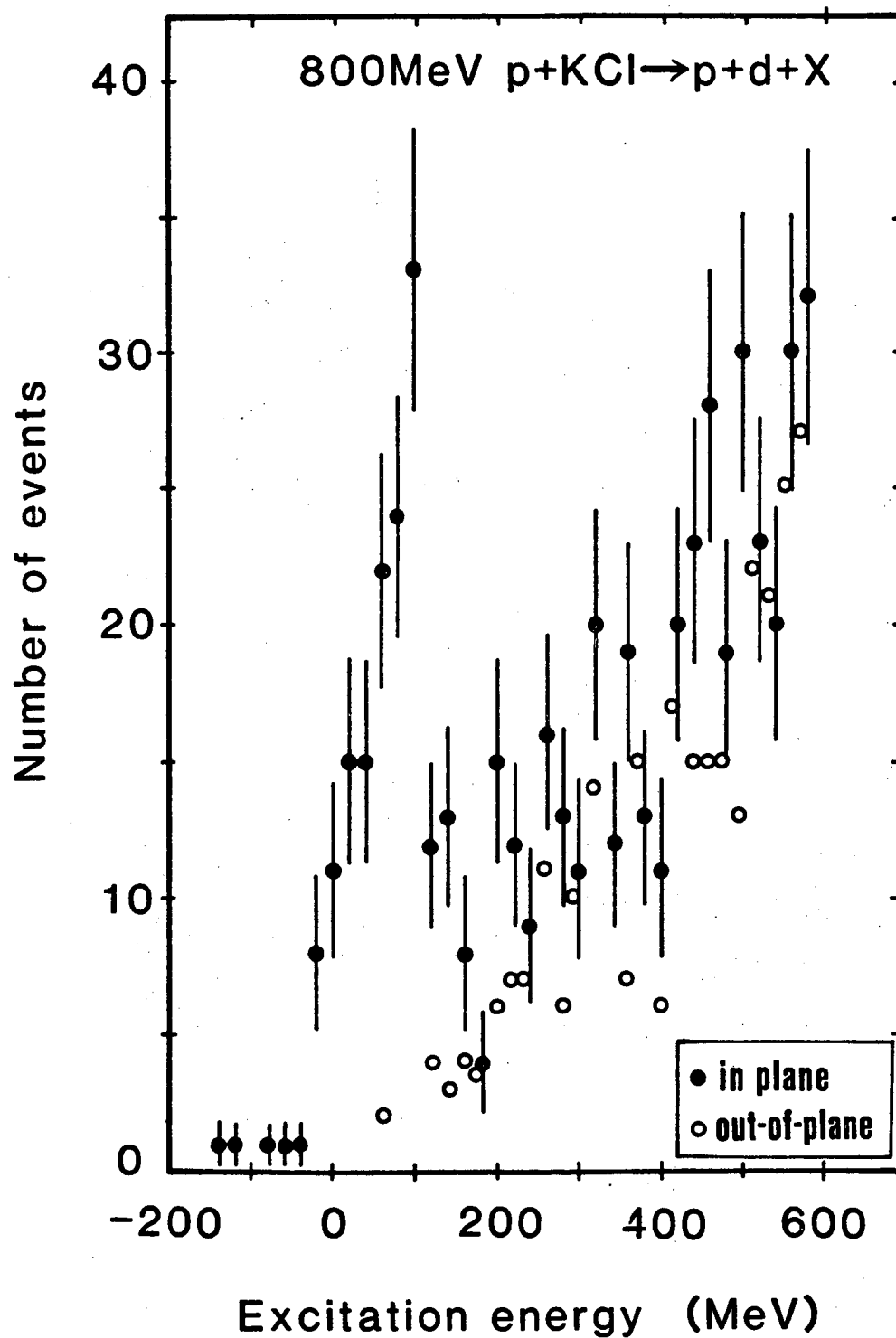
Fig. 11. Momentum-momentum scatter plots of proton-deuteron coincidence events. The mark "+" shows the kinematics of the p-d elastic scattering.

XBL 843-1115



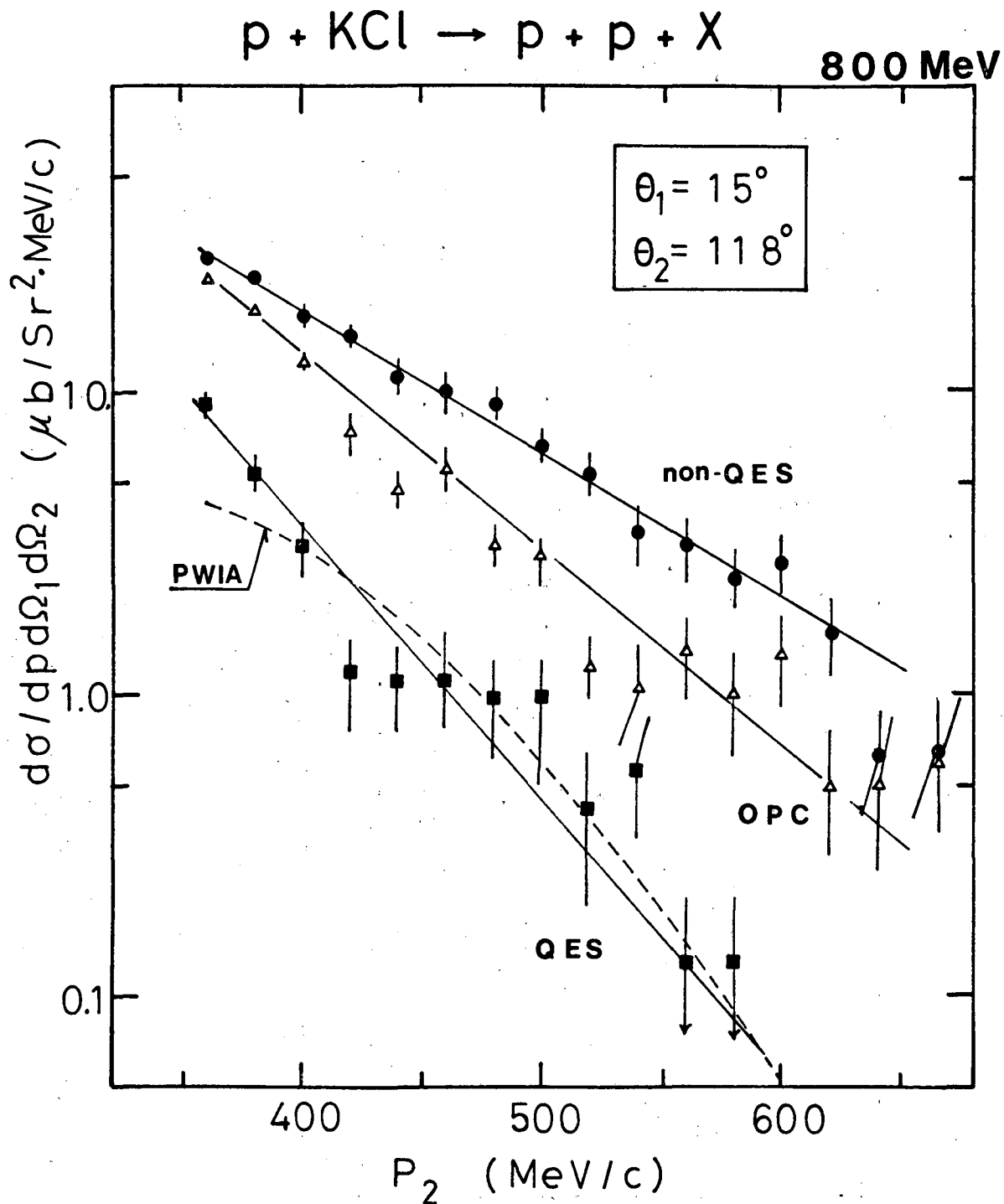
XBL 843-1114

Fig. 12. Distribution of the excitation energy(E_{ex}) of the residual nucleus for p-p events. Statistical errors are not shown for out-of-plane data but they have similar amount of errors as in-plane data. A peak near $E_{ex}=0$ shows the contribution from p-p quasi-elastic scatterings. Another peak at $E_{ex} \approx 450$ MeV is due to the instrumental kinematical limit.



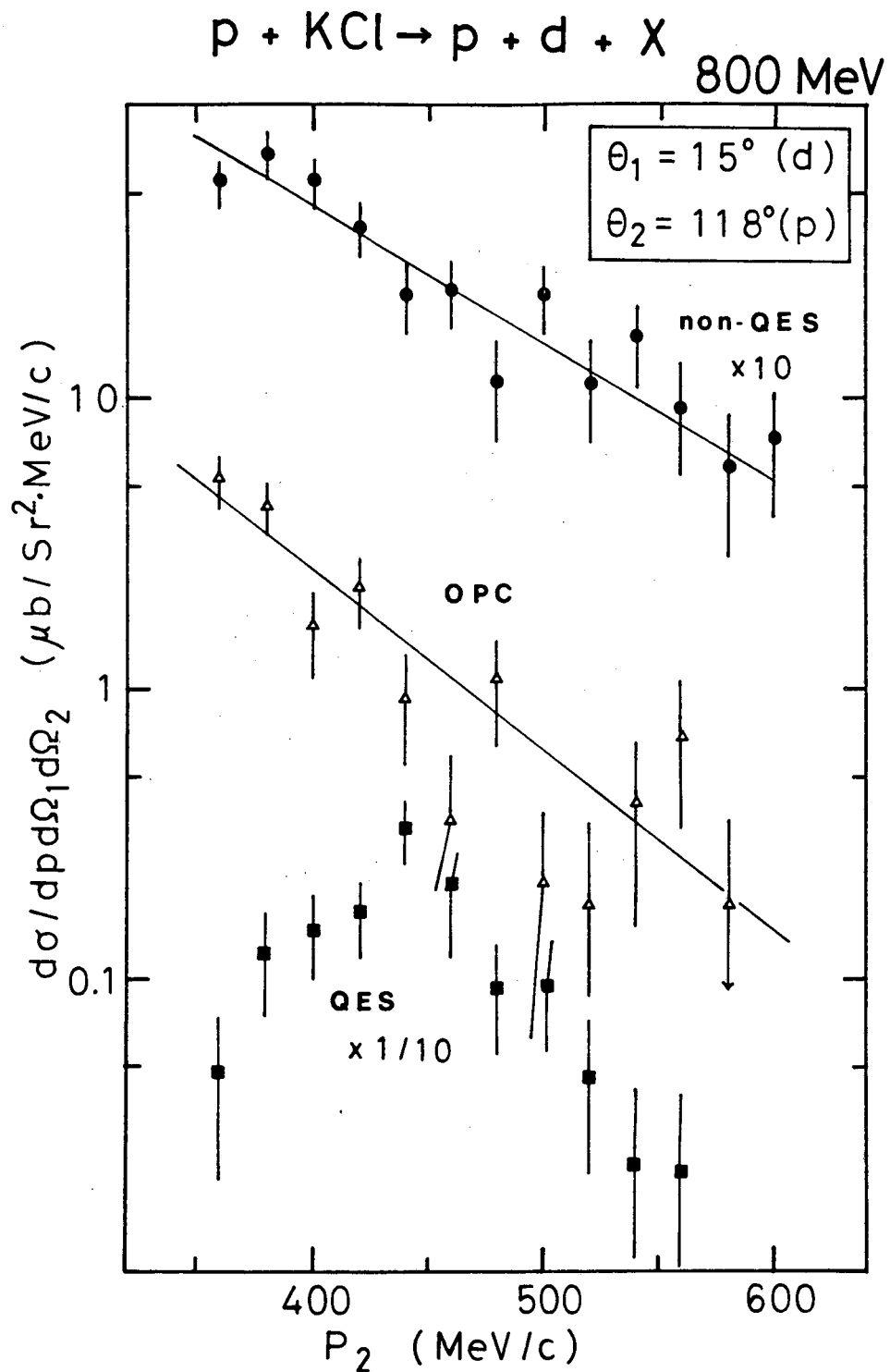
XBL 843-1113

Fig. 13. Distributions of E_{ex} for p-d events. A clear peak correspond to p-d QES is seen.



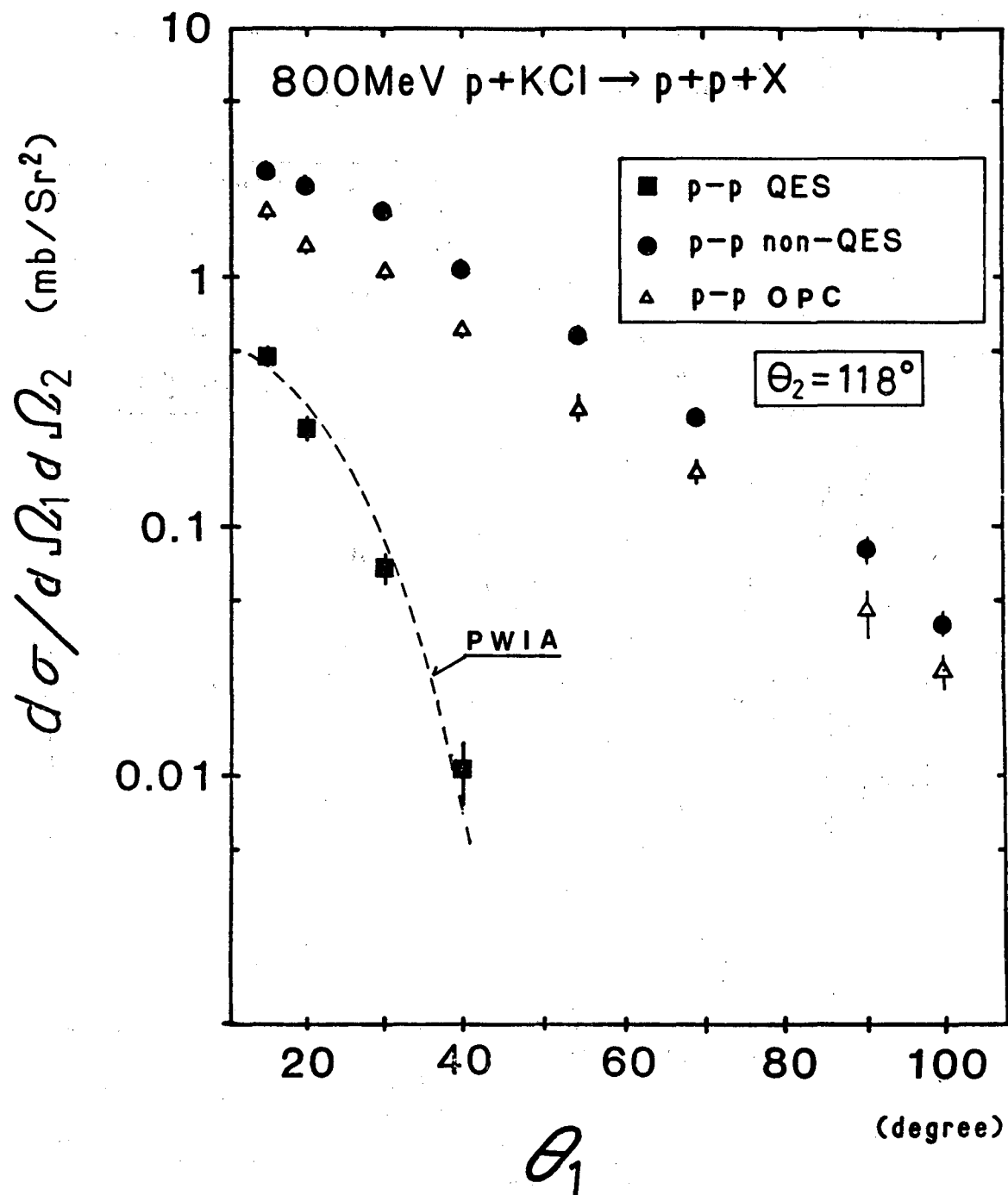
XBL 843-1112

Fig. 14. Spectra of the backward protons for the different components in $p+KCl$ collisions. Solid lines are the exponential fit to the data. Error bars in the figure show only statistical errors. A dotted curve shows the result of a PWIA calculations (see discussion in sec. 4.2).



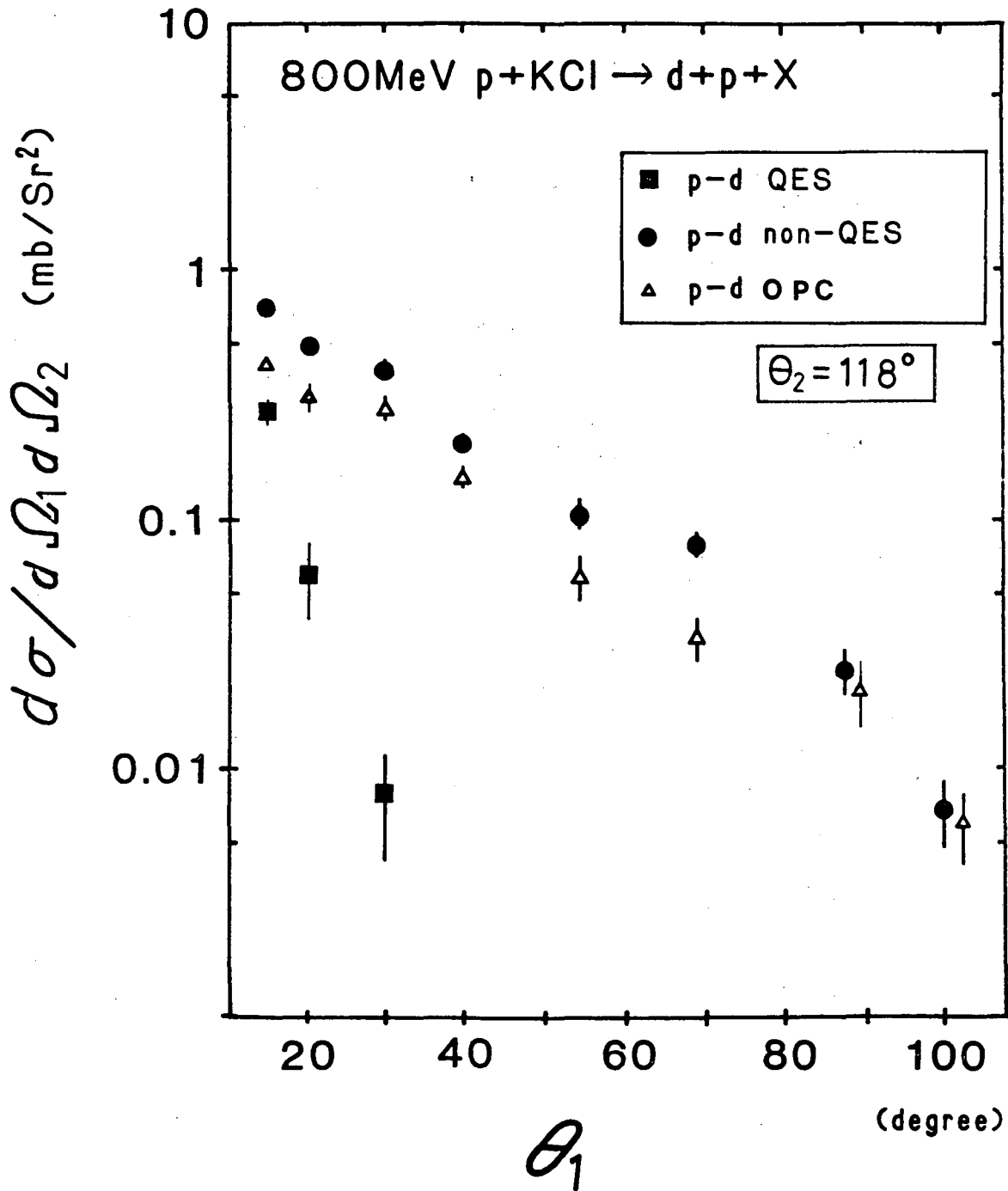
XBL 843-1111

Fig. 15. Spectra of the backward protons for the different components of p-d events. Solid lines are the exponential fit to the data. Error bars in the figure show only statistical errors.



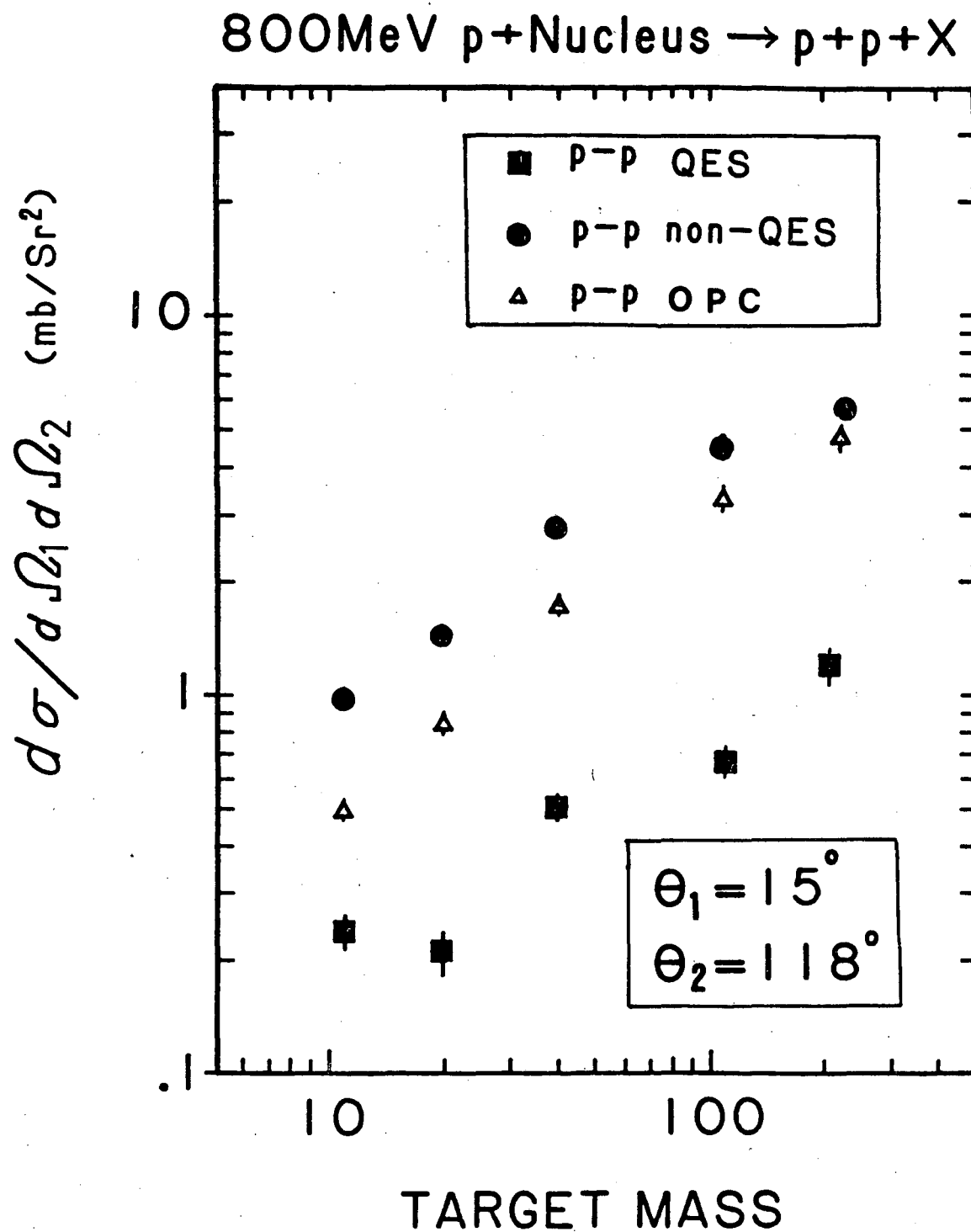
XBL 843-1109

Fig. 16. Angular distributions of protons in coincidence with backward protons at $\theta_2 = 118^\circ$. Error bars are only for statistical errors. A dotted curve shows the result of a PWIA calculations (see sec. 4.2).



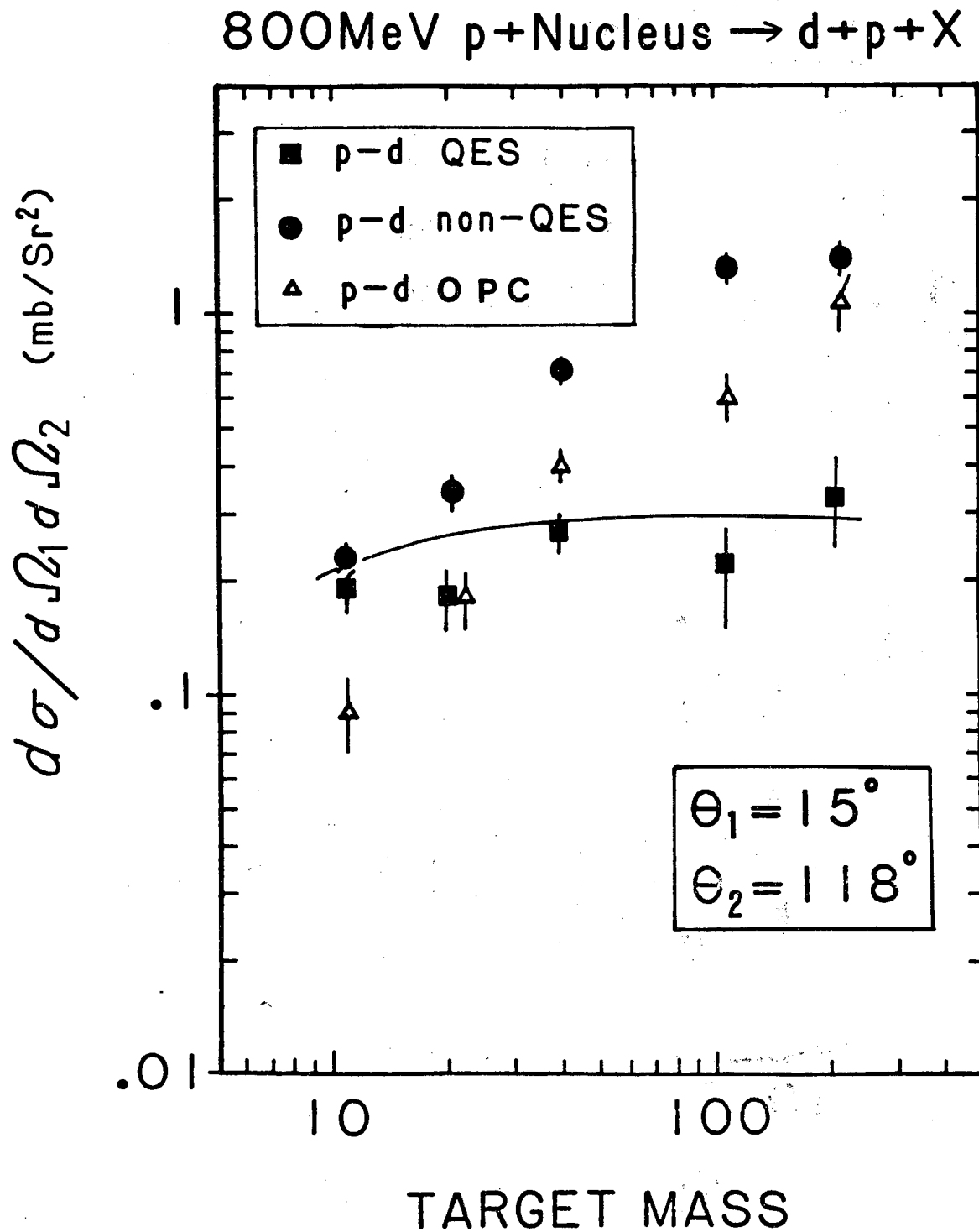
XBL 843-1110

Fig. 17. Angular distributions of deuterons in coincidence with backward($\theta=118^\circ$) protons. Error bars are only for statistical errors.



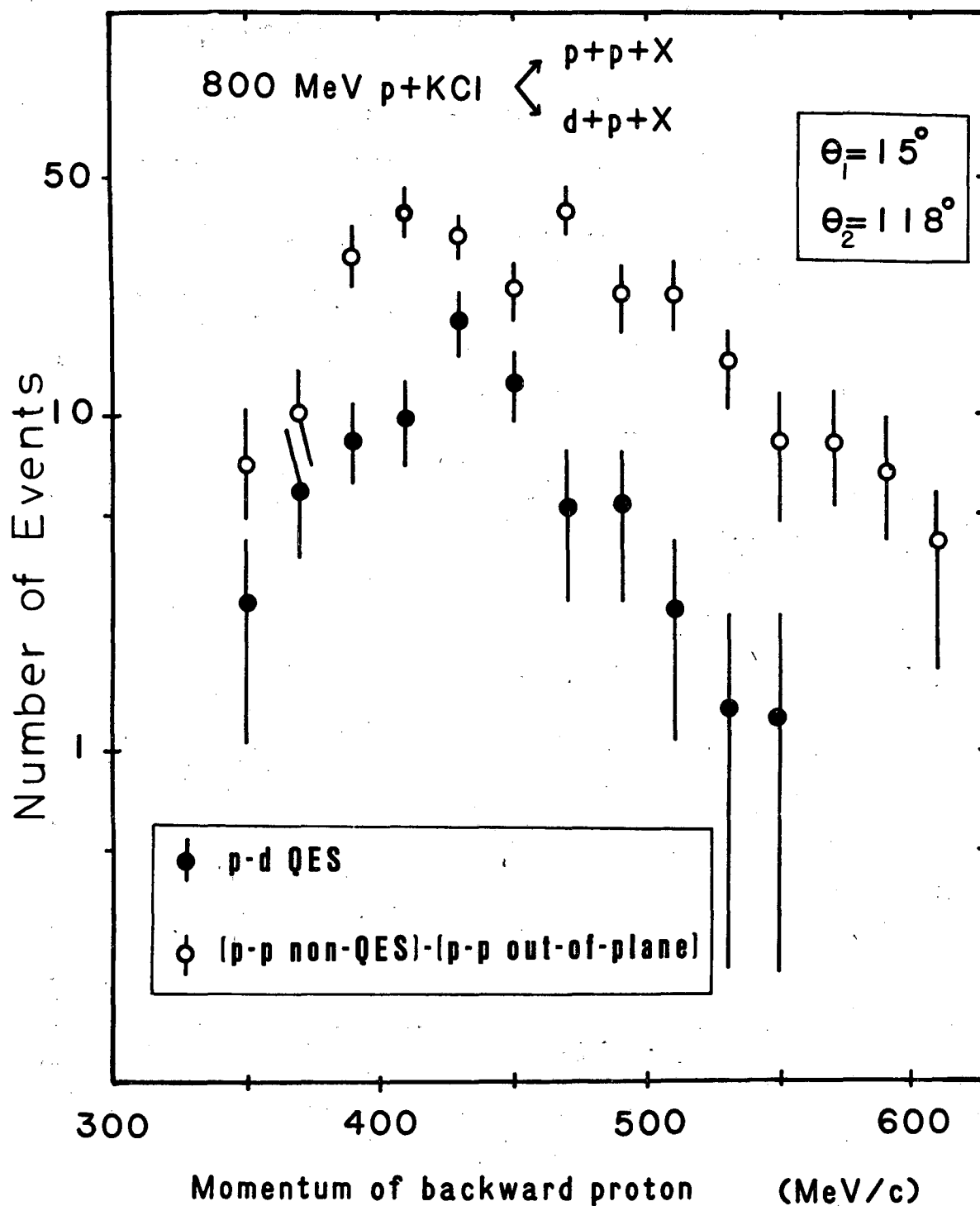
XBL 843-1108

Fig. 18. Mass number dependence of the p-p coincidence cross section. Error shown are only for statistical errors.



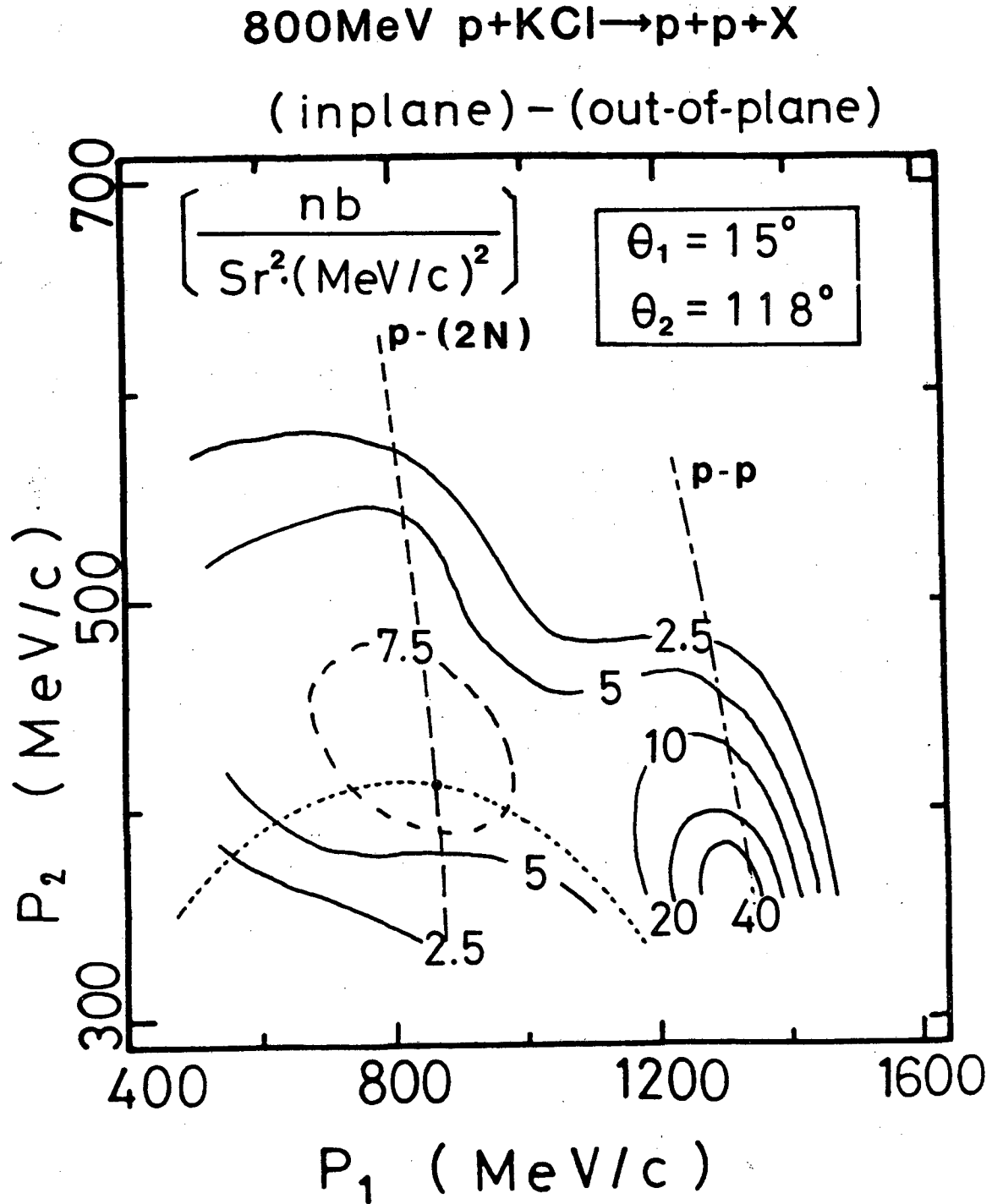
XBL 843-1107

Fig. 19. Target mass number dependences of the p-d coincidence cross sections. Error shown are only for statistical errors. A solid curve shows the result of the PWIA model calculation described in section 4.2.



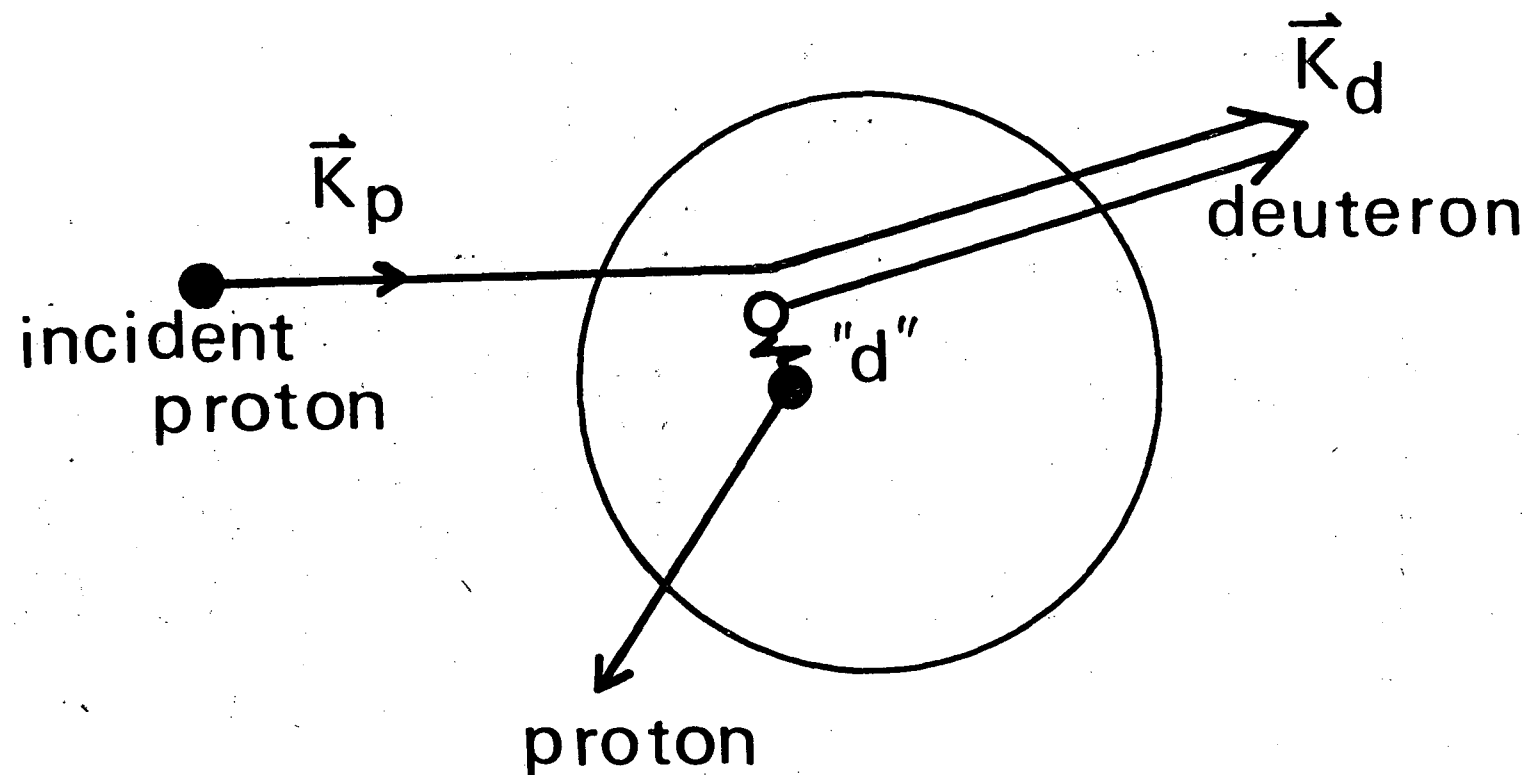
XBL 843-1106

Fig. 20. A backward proton spectrum of the "p-d QES" (solid circles) events and a difference spectrum between "p-p non-QES" and "p-p OPC" in the collision of p+KCl at the angles $\theta_1(=\theta_d)=15^\circ$ and $\theta_2=118^\circ$. Only statistical errors are shown in the figure.



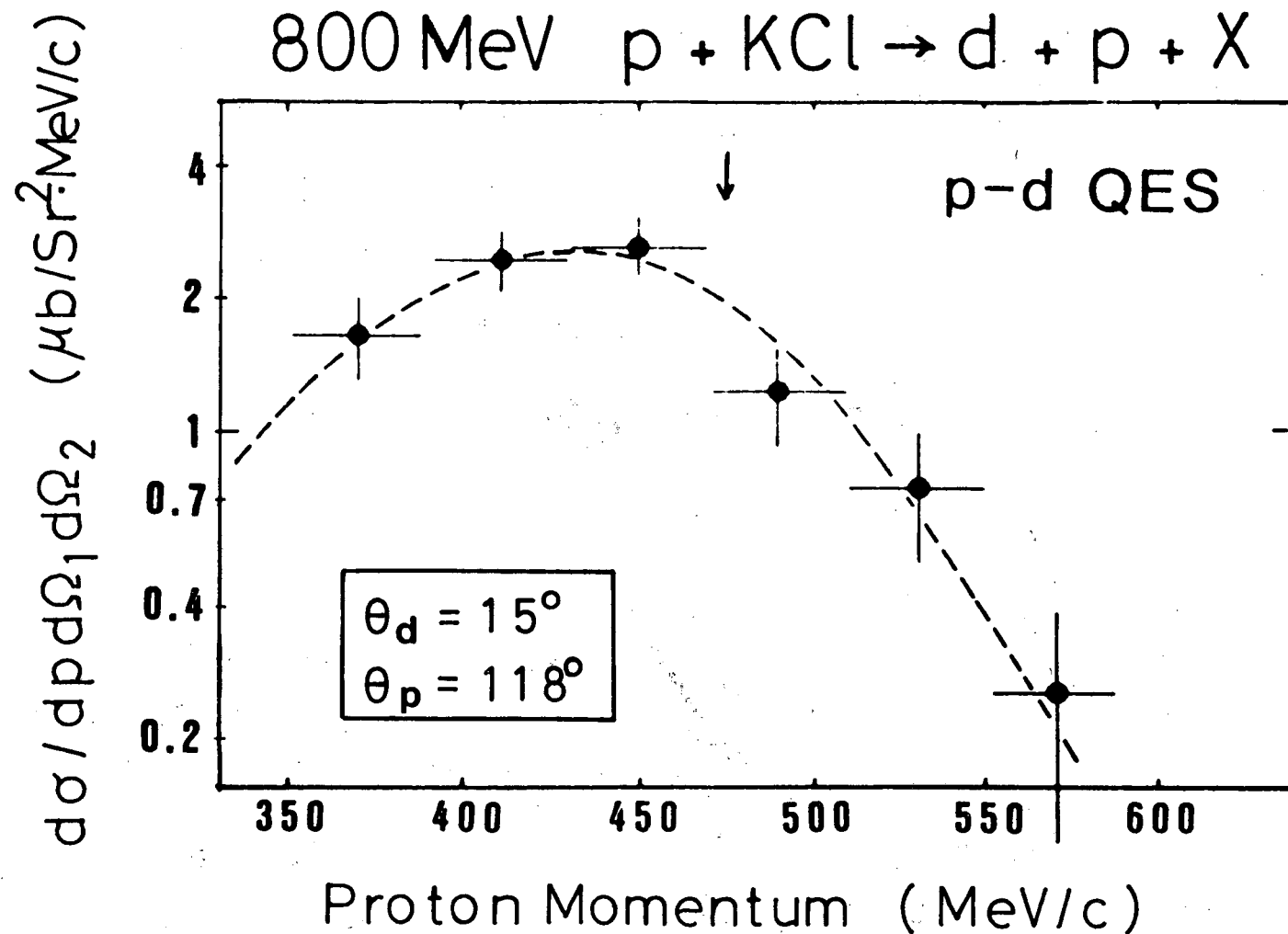
XBL 843-1105

Fig. 21. Contour line plot of the difference ("p-p in-plane" - "p-p OPC") of the double differential cross section. Kinematical loci of p-p QES and p-(2N) breakup reactions are also shown. A broad concentration of the events are seen around the p-(2N) breakup region.



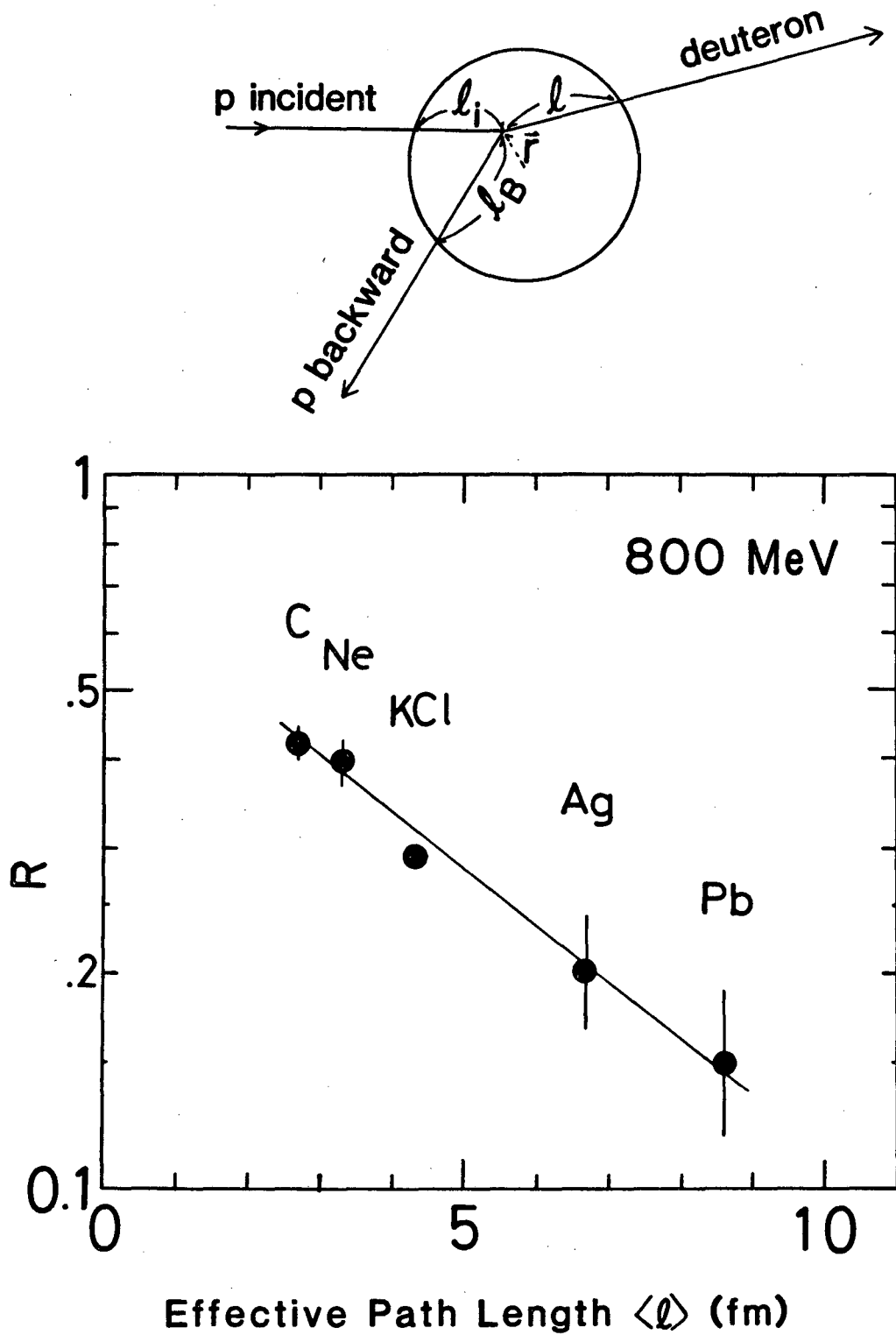
XBL 843-1104

Fig. 22. The reaction mechanism of p-d QES at large momentum transfer. Incident proton picks up a neutron which have a momentum $(K_d - K_p)$. The proton which was correlated with the neutron is emitted at a large angle.



XBL 843-1103

Fig. 23. Momentum spectra of backward protons associated with "p-d QES". A dashed curve shows the spectrum fitted to the data by a PWIA calculations. The momentum expected from p-d elastic scatterings are indicated by the arrow.



XBL 843-1102

Fig. 24. The cross section ratio(R) between p-d to p-p QES plotted as a function of the effective path length $\langle \ell \rangle$ of forward deuterons.

This report was done with support from the Department of Energy. Any conclusions or opinions expressed in this report represent solely those of the author(s) and not necessarily those of The Regents of the University of California, the Lawrence Berkeley Laboratory or the Department of Energy.

Reference to a company or product name does not imply approval or recommendation of the product by the University of California or the U.S. Department of Energy to the exclusion of others that may be suitable.

TECHNICAL INFORMATION DEPARTMENT
LAWRENCE BERKELEY LABORATORY
UNIVERSITY OF CALIFORNIA
BERKELEY, CALIFORNIA 94720